DETERMINATION OF STRESS CONCENTRATION FACTORS USING EXPERIMENTAL METHODS

by

Mark Warren Biegler

Thesis submitted to the Faculty of the
Virginia Polytechnic Institute and State University
in partial fulfillment of the requirements of the degree of

MASTER OF SCIENCE

in

Mechanical Engineering

APPROVED:

C. F. Reinholtz, Chairman

R. H. Fries

L. D. Mitchell

August 1988

Blacksburg, Virginia

DETERMINATION OF STRESS CONCENTRATION FACTORS USING EXPERIMENTAL METHODS

by

Mark Warren Biegler

(ABSTRACT)

Several experimental methods are examined for stress concentration factor determination. Tests are performed on a chosen 2-D specimen using strain gages, brittle coating, brittle specimen failure, photoelasticity, and Moire interferometry.

Results are compared to each other and to finite element analysis performed on the same geometry. Strain gaging and photoelasticity were chosen as the best methods for stress concentration factor determination.

ACKNOWLEDGMENTS

My sincere appreciation is extended to Dr. Charles Reinholtz for his constant guidance, friendship, and understanding. Dr. R. H. Fries and Dr. L. D. Mitchell are thanked for their continual support, guidance, and wisdom. Special thanks go to Dr. Daniel Post, Terri Edmondson, Mohammed Rezvani, and Joosik Lee.

* * * * * * * * * * *

For Mr. Biegler and one of his boys.

TABLE OF CONTENTS

LIST OF FIGURES

LIST OF TABLES

NOMENCLATURE

A_t	cross-sectional throat area
B'	Stefan-Boltzman constant
d	lattice spacing
e	surface emissivity
E	modulus of elasticity
f	fringe multiplication factor
F	grating frequency
K	general stress concentration factor
K_B	bending stress concentration factor
K_f	fatigue strength reduction factor
K_I	Mode I stress intensity factor
K_m	material constant for thermoelasticity
K_T	axial stress concentration factor
n	diffraction order
N	birefringence (fringe) order
p	radiant photon emmitance
P	load
PMMA	polymethylmethacrylate
q	notch sensitivity
r	root radius
R	resistance
S	strength (ultimate tensile)
S_A	strain sensitivity factor
SCF	stress concentration factor
t	specimen thickness

NOMENCLATURE (continued)

T	temperature
U	displacement
Z	final zero reading
α	half angle of intersection
Δ	differential
ε	strain
θ	angle of incidence
λ	wavelength
σ_{local}	local stress
$\sigma_{nominal}$	nominal stress
σ_{true}	true stress
σ_1, σ_2	principal stresses
2-D	two dimensional
3-D	three dimensional

CHAPTER 1
INTRODUCTION

Elementary strength of materials approaches can be used to find stresses in a uniformly shaped member. For example, stresses due to axial loads are found from $\sigma = P/A$ while bending stresses are found using $\sigma = \frac{Mc}{I}$. These relations are used to find average (nominal) stress remote from the point of load application. Such approaches do not, however, treat cases in which the member has some abrupt change in geometry. Unfortunately, most machine elements do contain such shape changes. These include threads, keyways, bolt holes, corners, and o-ring grooves. The localities surrounding these irregularities suffer stresses much higher than predicted by strength of materials approaches. In order to analytically find the true stress in such a region, one must multiply the calculated stress by a dimensionless "stress concentration factor." Algebraically

$$\sigma_{true} = K \sigma_{nominal} \tag{1.1}$$

where σ_{true} is the true stress in the region of geometric irregularity, $\sigma_{nominal}$* is the stress found by strength of material methods, and k is the stress concentration factor. The stress concentration factor (SCF) can be determined for a given geometry by finite element methods, theory of elasticity approaches, or experimental methods. The purpose of this thesis is to present, review and evaluate the various experimental techniques available for determining stress concentration factors.

For an isotropic material, the SCF is strictly a function of

*Nominal will be defined more precisely later on this thesis.

geometry and is therefore independent of type of material. This leads to much confusion about the application of the SCF. A SCF should be used in two general design situations, namely when a brittle material is used in a static or fatigue load situation and when a ductile material is used in fatigue loading. These two cases should be explained.

To explain a brittle material under static load, let us first consider a notched ductile tension member. As load is applied to the member, stress increases much more quickly at the notch than elsewhere. When the stress at the notch reaches the yield strenth of the material, local yielding occurs. Plastic strain now exists at the notch tip. Local strain continues until the stress is more uniform across the cross section. Such performance is possible because the ultimate strength of a ductile material is higher than its yield strength. This is not true in brittle materials. As a notched brittle specimen is loaded in tension, stresses increase non-uniformly, exactly as in the ductile case. The brittle specimen cannot yield locally at the critical point. Instead, failure occurs.

The use of a brittle material in a load bearing capacity causes many engineers to react with surprise. This application is not as rare as it may seem. "Ductile" materials are often used at temperatures well below their brittle transition temperature. These cases are not immune to SCF effects. An entire class of soviet submarines (alfa class) [1]* have pressure hulls built of titanium. Titanium under high hydrostatic pressure becomes brittle. SCF effects had to be taken into account in

*Numbers in brackets refer to citations listed at the end of this thesis.

the design of these undersea vessels.

In treating fatigue loading, stress concentration effects must be taken into account for both brittle and ductile materials. An engineer might wonder why local yielding does not occur at a stress riser in a fatigue-loaded ductile member. After all, this is why SCF's are not applied to statically loaded ductile members. There is no verified response to this question. The theory most often put forth [2] explains that local yielding takes too much time to occur in fatigue loading.

For whatever reason, SCF's are critical in fatigue calculations. The fatigue strength of unnotched specimen is divided by a fatigue-strength reduction factor K_f for a given notch. This gives the expected fatigue strength of the notched specimen. K_f is found from the relation

$$K_f = 1 + q\,(K_T - 1) \tag{1.2}$$

where q is the notch sensitivity and K_T is the geometric SCF. Fatigue strength is in this way dependent on stress concentration factors. Therefore, accurate predictions of fatigue life hinge directly on knowledge of stress concentration factors. A more complete explanation of fatigue stress concentration is contained in Shigley and Mitchell [3] and Sors [4].

CHAPTER 2
SURVEY OF AVAILABLE EXPERIMENTAL METHODS AND LITERATURE REVIEW

Many methods are available for experimental determination of stress concentration factors. These range from classical brittle failure to modern thermoelastic technology. In this chapter, each of 9 available methods are introduced. In most cases, operational theory of the methods is put forth. In addition, a survey of available literature is included. References explaining in-depth theory are reported. Also, a history of the use of each method in stress concentration factor determination is presented.

Chapter 2, Section I - Brittle Specimen Failure

Brittle specimen failure can be used to find both 2 and 3 dimensional stress concentration factors. The desired specimen shape is machined out of a brittle material. The specimen is then loaded according to design specifications. When the specimen fails, the stress at the failure point is known to be the strength of the material. Knowing loading and geometry, one can (in theory) use mechanics of materials to find the nominal stress at this point. The stress concentration factor is then simply the ratio of strength to nominal stress.

The procedure described above is deceivingly simple. There are a great many complications and limitations associated with this method. These should be explored.

Theoretically, this method works along the following scheme. There exists a notch of interest cut into a tensile specimen. As the load increases, stress at the notch tip increases. If the specimen is

ductile, local yielding occurs when the notch stress reaches some critical value. The stress is thus relieved. If the specimen were brittle, the strong atomic bonds do not allow such yielding to take place. When the stress at the notch tip overcomes the atomic bonds, the specimen ruptures locally. Ironically, the most apparent problem with the brittle failure method is the no-yield phenomena itself. All geometric imperfections, both macroscopic and microscopic, cause stress concentrations. As the radius of imperfection decreases, the SCF increases. Microscopic flaws can thus lead to high stress raisers in brittle material. Brittle failure may or may not occur at the point of interest. Resulting data would be of no use to a design engineer.

For similar reasons, it is not possible to know the strength of a given brittle material. Flaws cause the strength of materials like glass and cast iron to vary dramatically. The limit on the strength depends on the most severe flaw present in the specimen. Therefore, as specimen size increases, the probability of a higher SFC increases. As a result, strength is dependent on size. Since this method finds SCF's from the relation

$$K = \frac{S}{\sigma_{nom}} , \tag{2.1}$$

errors in strength information transform directly into SCF error.

Accurate knowledge of nominal stress is just as critical as strength information. For 2-D specimens, nominal stress can sometimes be found readily. However, as 3-D specimens become complicated, two problems arise. The first is actually defining nominal stress. For example, given a shell of revolution with a complex wall shape under

axial load, what is the "nominal area" or "average area" for stress calculations. Secondly, complex geometries do not yield simple mechanics of materials solutions. Numerical methods must be used, potentially inducing more error.

Finally, there is one other great limitation of the brittle failure method. Each machined specimen can be used only once and can determine only one piece of data at one point for the entire structure. This is obvious since after failure the stress distribution is drastically altered or eliminated altogether. This generally limits the use of this method to geometries which are inexpensive to fabricate.

Several experimenters have used brittle failure methods to derive a variety of data. Hetényi [5] credits Bach [6] with first using brittle materials in modern strength investigations.

M. M. Frocht, a pioneer in photoelastic work, failed brittle bakelite models to confirm photoelastic stress concentration work [7]. He found nearly the same SCF with each of the methods.

R. E. Peterson [8], in 1926, used plaster to paris specimens to examine stress concentrations. His work concerned flat bars with circular holes in tension and round bars with fillets in bending. Specimens were failed and the material strength was divided by nominal stress to find the SCF.

Much brittle failure has been done on the so-called angled elliptic notch problem. Williams and Ewing [9] loaded thin sheets of polymethylmethacrylate (PMMA) cut with angles notches. The axial loading caused failure in the brittle polymer. Load data was used to determine critical stress intensity factor as well as angle of crack propagation. Wu

et al. [10] carried on similar work on the same problem. These experimenters also used PMMA in their testing. Theocaris [11] previously discussed the use of PMMA in such a test. His experimental and analytical work revealed a small degree of yielding around a crack tip in PMMA. This would affect SCF calculation accuracy.

Cotterall [12] reported on the work of Hoek and Bieniawski. The experimenters used 6 in x 6 in x 1/4 in (15.24 cm x 15.24 cm x .64 cm) glass plates to do a 2-D failure analysis of plates with open cracks. Cotterell [12] examined stresses in similar glass plates with elliptical holes. All specimens were loaded in uniaxial compression to failure. Following this, Cotterell loaded the same types of specimens in tension to failure. He made conclusions as to the necessary force to cause failure for his geometry. This work is very similar to SCF work.

G. V. Eggeman [13] used brittle testing for certain 3-D work. His work concerned the shape of the failure envelope for biaxial stress fields. Test cylinders were machined from a fine grained graphite and loaded to brittle failure using a combination of internal pressure and axial loading. A method such as his could be used for 3-D SCF determination.

Chapter 2, Section II - Brittle Coatings

The brittle coating method is a relatively old method of experimental stress analysis. Developed in the 1930's [14], it can provide surface stress information accurate to within approximately 15%. A coating of brittle lacquer is applied to the part in question. It is assumed that this lacquer undergoes strain equivalent to the

specimen surface strain. Load is applied incrementally. When the coating cracks at the point in question, load is recorded. Coating calibration reveals the strain necessary to cause cracking.

The above information is interpreted as follows. Knowing surface strain at a given load, surface stress can be calculated. It is then assumed that stress is linearly related to load. Thus a load/stress relation can be created for the point in question. Many points can be investigated during each test run. This is the primary advantage of brittle coating over brittle fracture methods.

This tool may be applied to 2-D stress concentration factor determination. A specimen is machined in the desired geometry. The stress-riser region is coated with the brittle lacquer. The specimen is then incrementally loaded. Load at coating fracture is recorded. Calibration allows true stress, σ_t, to be found from

$$\sigma_t = \varepsilon E . \qquad (2.2)$$

Nominal stress, σ_{nom}, is found from analytical methods and the stress concentration factor is then σ_t/σ_{nom}.

The earliest American work using brittle coating was done by an M.I.T. graduate student named Greer Ellis. His advisor, Dr. A. V. deForest [14] published the first work on this method. It was a one page description of the method with a simple example. This paper was published in April of 1939.

Dr. deForest and Ellis [15] presented more work in January 1940. They reported their lacquer to crack near 1000 με. They also outlined calibration techniques as well as specimen coating methods. They credit a German named Dietrich with the first attempts in this field. deForest

and Ellis published yet another paper [16] in 1942. This paper examined effects of humidity, creep, coating thickness, and temperature on test results.

Hetenyi and Young [17] applied the method to analyze various machine elements. They showed it to be useful to compare different design options. Durelli and Kobayashi [18] used brittle coatings in conjunction with photoelastic work. Their brittle coating work was qualitative in that it was used to find principal stress directions.

Chapter 2, Section III - Strain Gages

In 1856, Prof. William Thomson (Lord Kelvin) discovered that the resistance of iron and copper wires increased as the wires were strained. This work was presented to the Royal Society of London. Thomson's work was followed by P. W. Bridgman in the United States. His work was published in 1923. A relation for the change in resistance of a single strand of uniform conductor was defined

$$\frac{dR}{R} = S_A \varepsilon \ . \qquad (2.3)$$

In this relation, S_A represents the strain sensitivity factor, R is conductor resistance and ε is the applied strain. If an experimenter knew the strain sensitivity and could measure a change in resistance, strain could be determined. This enormous experimental potential was recognized and the first commercial strain gage became available in the mid-1930's. Single strand gages have evolved into etched foil serpentine gages which have a large active gage length for their small area.

Strain gages can be used to find stress at the root of a notch and can with proper care be used to find SCF's. This type of work has been

carried out by several authors. Kikukawa [19] did exactly this in using strain gages to find stress concentration factors for notched 2-D specimens. He compares his work to analytical results.

A problem concerning the use of strain gages in this application involves the unit gage length. The gage simply averages strain under it. This means that peak strains are camouflaged by neighboring lower strains. This problem was addressed by Watanabe and Izumi [20] in 1962. They fabricated a gage of variable gage length. It was mounted in a notch and used it to measure strain. Readings were made as the active length was shortened. Measured strain increased with each step. The data was then extrapolated for a gage of minimum length.

More recently, Dally and Sanford [21] applied strain gage technology to fracture mechanics. Their interest was in determining stress intensity factors (K_I) for a crack tip. This paper contains procedures for locating and orienting gages near cracks to give crack stress intensity factors. The authors also developed expressions for strains near the crack tip.

Chapter 2, Section IV - Photoelasticity

Photoelasticity has been a traditional workhorse in determining stress concentration factors. Practical work dates from the early 1920's. This method can be used for both 2-D and 3-D work. This section first gives a brief history and literature review of photoelastic stress concentration work. Next, it gives a simple overview of the method and references detailed explanations.

Literature Review - Photoelasticity

In 1816, David Brewster [22] discovered that certain optically isotropic materials become optically anisotropic when stressed. This was the first step toward modern photoelasticity. In 1841, Neumann [23] derived the stress optic law in terms of strain. Maxwell [24] followed-up this work and in 1853 published the stress optic law in terms of stress. These three equations relate change in directional indices of refraction to principal stresses and material constants. These equations are the basis for modern photoelastic analysis.

Frocht [25] credits Coker [26] with the first American work using photoelasticity in an engineering application. Tuzi [36] is credited with the first work using frozen section photoelasticity. This work was published in Japan in 1927.

Frocht himself was a pioneer in the field. His paper [27] "Photoelastic Studies in Stress Concentration" examined various holes, grooves and fillets in tension, compression, and bending. Similar work is carried out by Frocht [28,29,30,31,32]. In these papers, Frocht and his co-authors have catalogued a great number of 2-D stress concentration factors.

Since Frocht, 2-D photoelasticity has been used by various individuals to find SCF's. In 1961, Durelli and Riley [33] concerned themselves with the 2-D SCF of a circular hole in a dynamically loaded plate. Dynamic loading was applied with an impact to one edge of the plate. They compared their results to the Kirsch solution and found fairly accurate correlation.

In the field of fracture analysis, 2-D photoelastic work has been

done on crack tip stress intensity factors. In 1975, Theocaris and Gdoutos [34] published a paper on Mode I stress intensity factors. This work was done photoelastically and is very similar to the work of interest in this paper.

More recently, Hanus and Burger [35] investigated the interaction of an elliptical hole and a nearby free edge. Their work used 2-D photoelasticity to determine SCF's.

Meanwhile, the field of frozen stress and 3-D photoelasticity were developing as well. Frocht [25] cites Tuzi [36] of Japan with the first quantitative work using frozen stress patterns. Tuzi quenched phenolic bars from 130°C. He then sliced the bars and photoelastically examined the preserved stress pattern. In December of 1938, M. Hetenyi [37] published a paper describing theory and procedures for frozen-section photoelasticity. Hetenyi showed that sawing a bakelite specimen does not disturb its preserved birefringent pattern. Hetenyi shows stress contours in tensile specimens with semi-circular notches loaded from pins. Hetenyi then examines cut frozen specimens. The patterns were undisturbed.

In 1940, Drucker and Mindlin [38] reported problems encountered in 3-D photoelasticity. They also presented methods for analysis of whole planes as opposed to point by point strain analysis.

In 1943, Max Frocht [39] published a lengthy treatise covering a wide range of subjects integral to 3-D photoelasticity subjects. He presented "[methods for] loading, slicing, improvement of boundary visibility, a discussion of time stresses, and methods for the determination of the fringe order and fringe value in a model with a static or frozen

stress pattern." He went on to present results for certain 3-D SCF's as well as develop a correlation between 2-D and 3-D SCF's. He shows 3-D factors to be slightly higher than 2-D factors for equivalent geometric ratios (such as root radius).

In 1950, Leven [40] reported on 3-D SCF's in shaft keyways. He compared his results to theory of elasticity solutions. The following year, Leven and Hartman [41] detailed SCF's in flat bars and shafts of varying cross section.

Fessler and Roberts [42] experimented with 3-D photoelasticity and transverse shaft holes. Their specimens were made of araldite casting resin B which were axially loaded during the stress freezing cycle. In 1971, Marloff et al. [43] explored the general aspects of and procedures for 3-D stress intensity factor determination by this method. Sanford and Beaubien [44] published a paper comparing this type of work to finite element analysis.

More recently, Smith and his associates [45,46,47,48] have applied frozen section photoelasticity to crack-tip stresses. This work was carried out in the fracture Mechanics Laboratory at Virginia Polytechnic Institute and State University.

As discussed earlier, Brewster discovered the phenomenon of birefrengence in certain stressed materials. This is the basis of photoelasticity. Post [49] described the method along the following lines. Take, for example, a specimen model made of photoelastic material. When the material is stressed, light passing through the model is divided into two components. The first component has plane of polarization in the σ_1 direction and the second component has a plane of

polarization along σ_2. Due to the birefringence, light along σ_1 travels faster than along σ_2. This delay causes a shift in phase between the two light components. A polarizing filter then merges the two components into a single plane of vibration. Since there was a shift in phase, N, between the components, optical interference occurs. If N is an integer number of cycles (N = 0,1,2,3,...) the components reinforce one another. This results in a bright zone. Where N is 1/2 order, (N = 1/2,3/2,5/2,...) interference is destructive and a dark fringe occurs. Between light and dark fringes, varying intensities of grays occur. This phenomenon is expressed in the equation (derived from stress optic law):

$$\sigma_1 - \sigma_2 = \frac{f}{t} N \tag{2.4}$$

where f is the fringe multiplication factor, t is the specimen thickness, and σ_1 and σ_2 are principal stresses. (σ_3 is defined as zero, whether the load is tensile or compressive.) From this equation, one can find $(\sigma_1 - \sigma_2)$. At a free surface, $\sigma_2 = 0$. Therefore one can find σ_1 directly.

The above paragraphs speak in theory and generalities about the production of a fringe pattern. Specifics of polariscope design and specimen loading should be addressed.

A schematic of a circular polariscope is depicted in Fig. 2.1. The monochromatic light source can be a laser or filtered white light. Vapor lamps can also be acquired which produce light in a sufficiently small bandwidth. Light enters the polarizer. This element polarizes the light along its polarizing axis. This surviving light passes to the quarter-wave plate. This element is equivalent to a specimen with

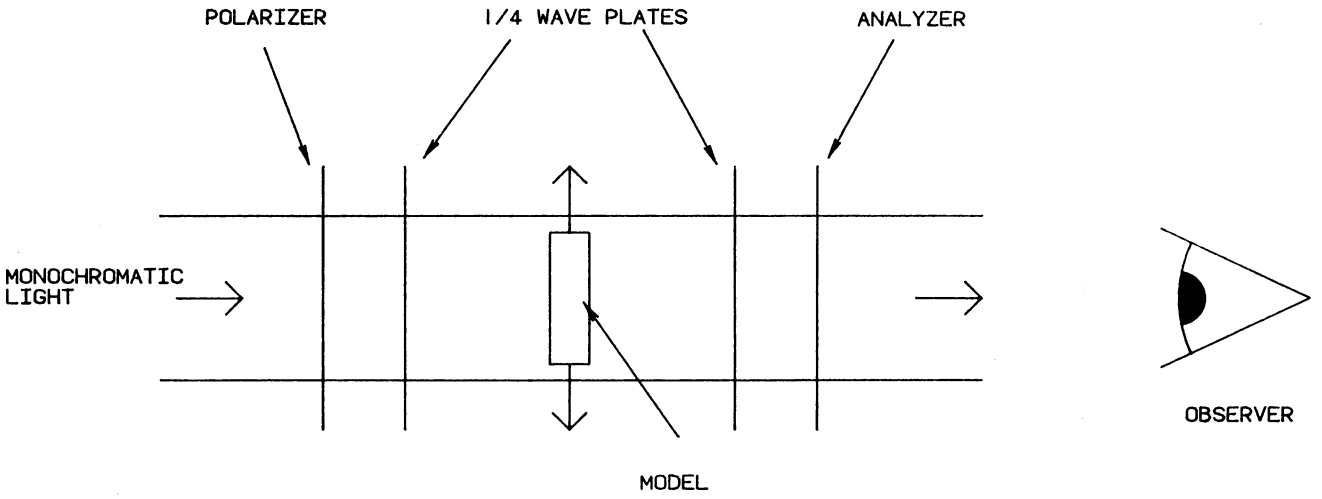

FIGURE 2.1 SCHEMATIC OF CIRCULAR POLARISCOPE

uniform birefringence order of N = 1/4. Its principal axes are at plus and minus 45° to the axis of the polarizer. This element simply divides light uniformly along 2 axes for model illumination. Light then passes through the model and gathers the above-mentioned stress information. The second quarter-wave plate has axes 90° to the first. It removes "stress" information added by the first. The analyzer polarizes incident light. This allows for the optical interference discussed above. If the axis of the analyzer is parallel to that of the polarizer, a light-field background results. If the axes are at 90°, a dark field results.

Two-dimensional photoelastic specimens are loaded while the fringes are observed and photographed. A specimen model is fabricated from photoelastic material and field loading is simulated in the polariscope.

The "loading" of a 3-D photoelastic model is done in a different manner. Materials for this method are thermosetting polymers that behave according to multi-phase theory. Burger [50] describes the process in this way. The material is like a sponge whose pores are filled with wax. When the composite is heated, the wax becomes viscous while the sponge remains elastic. Loading causes elastic deformation. The load is held constant as the specimen is uniformly cooled back to a firm solid. The model can then be sliced to examine planes of interest. These slices can be put in the circular polariscope described earlier. Burger [50] described both 2-D and 3-D photoelasticity in great detail.

Chapter 2, Section V - Moire Interferometry

While the photoelastic method has been in use for quite a while, the optical method of Moire interferometry is relatively new. In recent years, this has become a very sensitive and accurate method, able to routinely measure in-plane displacement on the order of 10^{-5} inches. Spatial resolution is also quite high. This high resolution means information is available for a great many points in a small area. It utilizes concepts common to geometric Moire and classical interferometry. A brief discussion follows.

The word Moire comes from the French for watered silk. When fabrics such as this are overlaid, bands of interference (light and dark) are seen. (Classical) Interferometry uses shifts in light phase to make linear measurements. It is from these two origins that this technique was named.

Guild [51] did early work with the concept of Moire interferometry. His efforts sketched the outline of present understanding. Early quantitative work was done by Underwood and Kendall [52] in 1969. In the past 10 years, available technology has made Moire interferometry more practical as well as more accurate. In 1980, Post [53] published an explanation of interferometric theories. In this he included Moire and showed examples of experimental work. Hiatt [54], working under C. W. Smith and Post, applied this methodology of stress intensity work at crack tips. He compared his work to previous 3-D photoelastic work and found about 5% difference in results.

From 1981 to 1983, the technology advanced rapidly. Basehore and Post [55] produced more specifics on in-plane measurements. In this

paper, they also presented a method to use Moire interferometry to measure out-of-plane displacements. Nicoletto [56] applied the method to fracture mechanics. He published a guide for determining stress intensity factors by optical methods. In 1982, Sciammarella [57] wrote a useful review of Moire technology.

Several papers have been presented which combine Moire interferometry with other experimental methods. Watson and Post [58] suggested Moire as a method to calibrate strain gages. Smith et al. [59,60] used an ingenious hybrid combination of 3-D photoelasticity and Moire interferometry.

The method has been used to determine crack tip displacement [61] as well as displacements at dovetail notch tips [62].

The following is a simple description of the Moire interferometric method. An elegant, readable description can be found in Post [63].

When two light beams of the same wavelength and common polarization intersect as in Fig. 2.2, a particular optical interference pattern results. Walls of destructive (dark) and constructive (bright) interference are produced. The frequency of this pattern is related to the angle, 2α, between the intersecting beams. The frequency, F, is

$$F = \frac{2}{\lambda} \sin\alpha \tag{2.5}$$

for light of wavelength λ.

Concepts of grating diffraction are also necessary for this explanation. Take, for example, a beam of light illuminating a transmission grating of frequency F (see Fig. 2.3).

Light is scattered by the grating into component rays. These rays are numbered from 0 (passing unaffected through the grating) in a

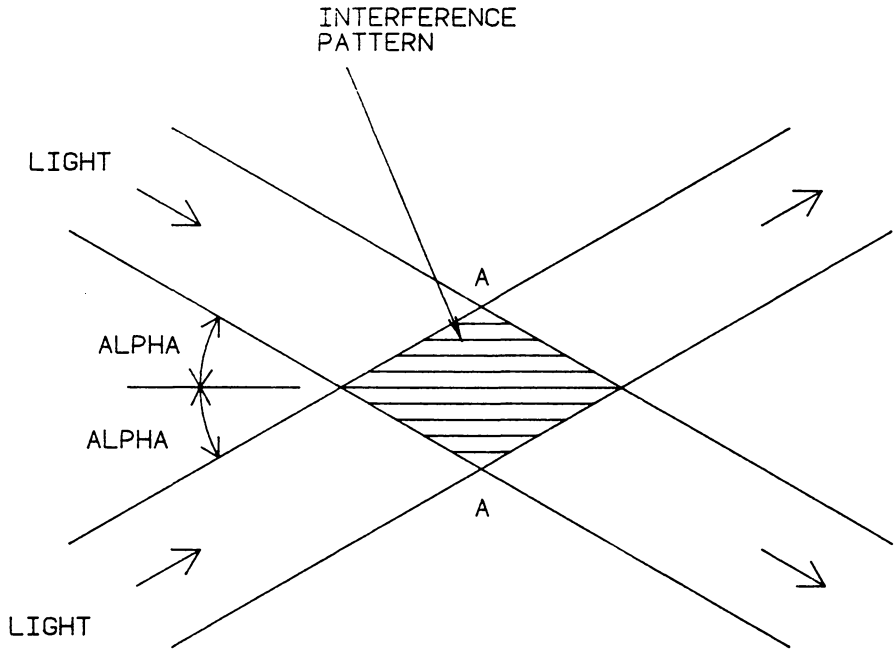

FIGURE 2.2 INTERFERENCE OF NON-PARALLEL BEAMS

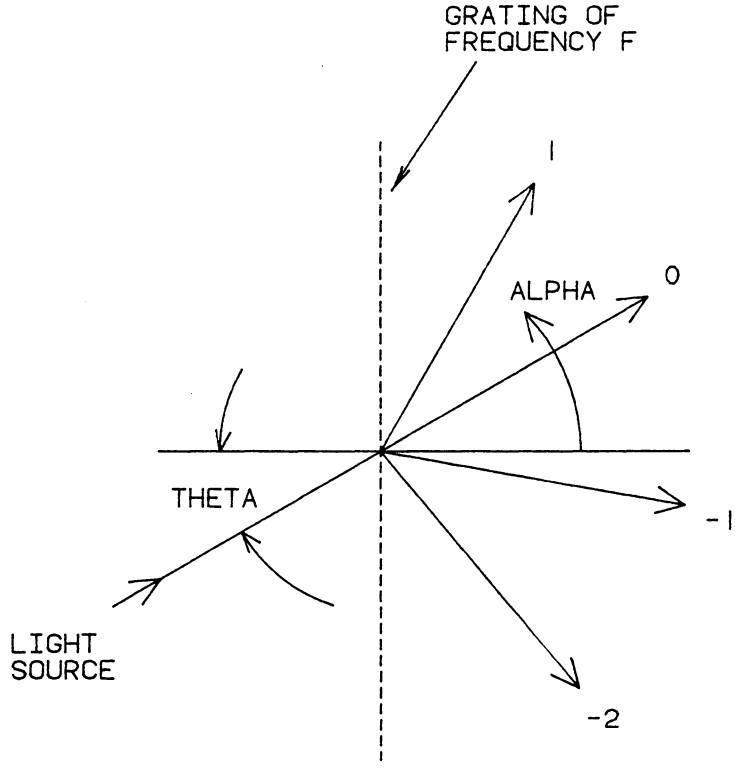

FIGURE 2.3 OPERATION OF TRANSMISSION DIFFRACTION GRATING

positive manner counterclockwise. The angle α, of the emerging m^{th} ray, is found from

$$\sin\alpha_m = m\,\lambda F + \sin\theta \ . \tag{2.6}$$

If two gratings of proper frequencies F and F/2 are put in series, the result is like that shown in Fig. 2.4. If the second grating is given a positive (tensile) strain ε, its frequency becomes $\frac{F/2}{1+\varepsilon}$. The rays emerging from the second grating are no longer parallel, and the condition of Fig. 2.2 exists. Each fringe, N, represents a zone of constant in-plane displacement (perpendicular to the grating lines). This displacement, U, is

$$\Delta U = \frac{\Delta N}{F} \ . \tag{2.7}$$

Digitizing techniques can then be used to find strain, ε, according to the relationship

$$\varepsilon = \frac{\partial U}{\partial X} \doteq \frac{\Delta U}{\Delta X} \ . \tag{2.8}$$

Although this method finds displacements rather than stress or strain, it holds great promise for future SCF work. A vast number of publications by the Virginia Polytechnic Institute and State University Photomechanics Group [48-51,54-58] have demonstrated this fact. This method will be demonstrated in Chapter 5.

Chapter 2, Section VI - Other Methods

Many methods of experimental stress analysis are available. Most of these can in some way be used to find stress concentration factors. A number of these methods should be briefly mentioned. These methods

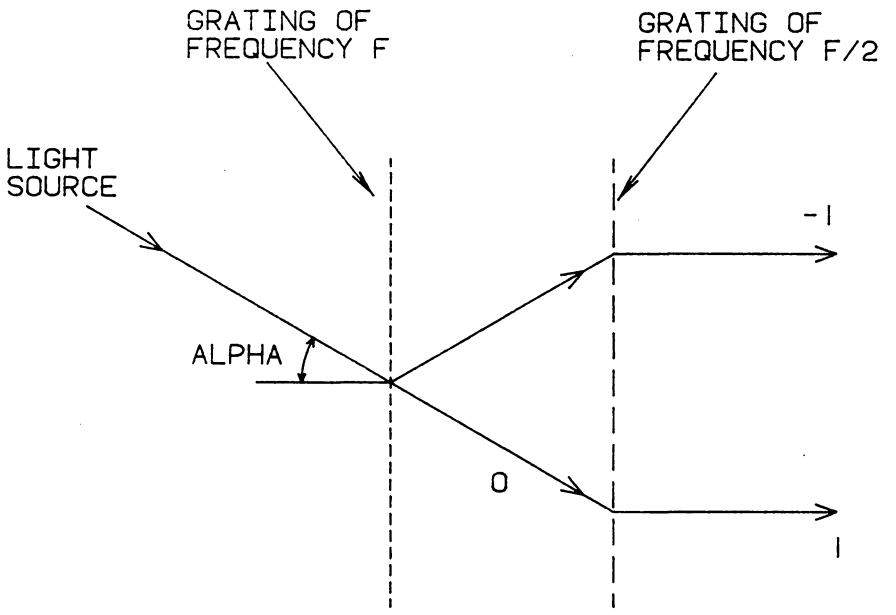

FIGURE 2.4 DUAL GRATING INTERACTION

include thermoelasticity (S.P.A.T.E.®) holographic, interferometry, x-ray diffraction techniques, and electron emission.

The basis of S.P.A.T.E.® (Stress Pattern Analysis by Thermal Emission) dates back to the 19th century when Lord Kelvin discovered that pressurization of a gas results in gas temperature change. Equivalent results occur when a solid member is stressed. The S.P.A.T.E.® system measures this temperature change and determines stresses from it.

Oliver [64] explains S.P.A.T.E.® theory and credits Biot [60,61,62] with developing the equation

$$\Delta T = - K_m T \Delta\sigma \tag{2.9}$$

where ΔT is temperature change, K_m is a material constant, T is a reference temperature, and $\Delta\sigma$ is the stress change. This equation holds for homogeneous, isotropic materials under adiabatic loading. It should be noted that this temperature change is not a hysteresis effect. Use of this relation to find stress requires that the experimenter measure a temperature change in the specimen. Early thermoelastic work did this by use of thermocouples. This type of instrumentation is cumbersome and offers few advantages over strain gaging.

Modern infrared technology has allowed the thermoelastic method to become a non-contacting, scanning, and more versatile means of stress analysis. Infrared sensors detect infrared radiant photon emittance, (p). This emittance is a function of temperature. Present S.P.A.T.E.® systems utilize such sensors. With proper substitution (Stefan-Boltzman

---

S.P.A.T.E.® is a registered trademark of Ometron Corporation, Herndon, Virginia.

Law), Eq. (2.9) becomes

$$\Delta p = -3\ e\ B'\ T^3\ K_m\ \Delta\sigma \qquad (2.10)$$

where e is surface emissivity and B' is the Stefan-Boltzman constant.

Equation (2.9) specifies adiabatic specimen conditions. This is obviously not possible. To overcome this, cyclic load is applied to specimens in the range 0.5 Hz to 20 kHz. A load reference signal is compared by S.P.A.T.E.® to the infrared signal. This allows S.P.A.T.E.® to filter out certain non-stress induced temperature changes. Loading frequency depends on specimen heat-transfer properties.

Equation (2.10) shows Δp to be directly proportional to emissivity, e. This means the specimen surface must have uniform emissivity. Ometron Corporation (the S.P.A.T.E.® manufacturer and marketer) suggests that the specimen surface be sprayed with flat black paint under these conditions. Errors due to emissivity variation are on the order of 2%.

Oliver [64] reports spatial resolution of this method to be near .5 mm. Mountain and Webber [68] give an explanation of S.P.A.T.E.® as well as experimental results. They report spatial resolution of 1 mm and sensitivity of near 300 psi (2.07 MPa). Stanley and Chan [69] offer a critical appraisal of S.P.A.T.E.® technology. They give the method a favorable review.

Since this method requires visual contact with the plane of interest during cyclic loading, the method is not obviously appliable to 3-D SCF determination. However, it does show great promise for work with 2-D specimens. Initial costs of S.P.A.T.E.® equipment are high ($185,000) but data can then be gathered with ease.

Holographic interferometry can be used to find both 2-D and 3-D

stress concentration factors. A general explanation of holographic methods will be followed by suggested methods for SCF work.

A specimen and mirror are arranged side-by-side as in Fig. 2.5. When illuminated from the light source, light scatters from the specimen in all directions, including toward the observer. Light reflects from the mirror as shown. Optical interference occurs in the zone of intersection of these two reflected beams. A photographic plate is exposed in plane A-B to record the interference pattern. Upon processing, the plate becomes a diffraction grating. If the grating is then re-inserted along AB and if the specimen removed, the observer still sees an exact 3-D image of the specimen. This is a hologram.

If both the specimen and grating are in place, the observer still sees one image, in the specimen plane. This is because the light (from the mirror) diffracted by the grating is in phase with the light reflected by the specimen. Now imagine that a point on the specimen suffers out-of-plane displacement of one-quarter λ. That is, the point is moved $\lambda/4$" away from the observer. The light reflected by this point will now be out of phase with the corresponding light from the grating. Since the beams are 180° out of phase at this point, complete destructive interference will occur. The observer will see no light from this point (this is a "dark fringe"). Such displacements of odd 1/4 order ($\frac{\lambda}{4}$, $\frac{3\lambda}{4}$, $\frac{5\lambda}{4}$, ...) result in dark fringes. Displacements of one-half order (0, $\frac{2\lambda}{4}$, $\frac{4\lambda}{4}$, $\frac{6\lambda}{4}$, ...) result in light fringes.

This method can be used to find 2-D stress concentration factors. The apparatus is the same as that of Fig. 2.5. Take, for example, a notched specimen. The hologram is created in the no load state. As the

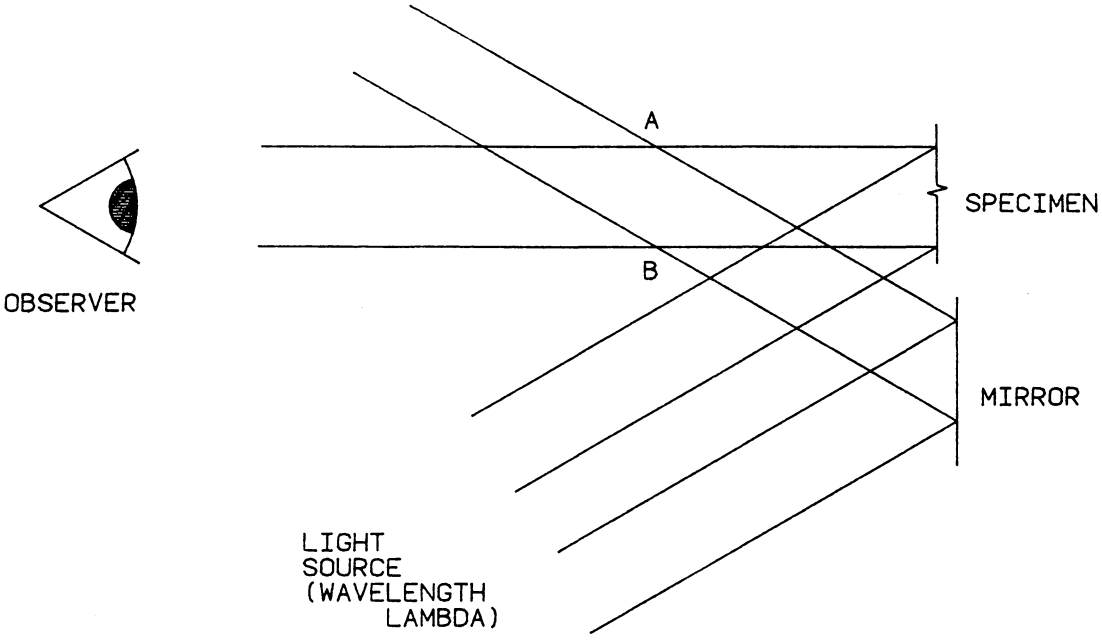

FIGURE 2.5 HOLOGRAPHY SCHEMATIC

specimen is then axially loaded, poisson effect will cause points on the visible surface to move away from the observer. The resulting interference pattern seen and photographed by the observer reveals the strain distribution on the specimen surface, including the notch region. The SCF is found simply from here.

Similar methods can be used to find 3-D SCF's, but specimen creation is tricky. A 3-D model is machined from 3-D photoelastic material. Stresses are applied and "frozen" exactly as if 3-D photoelastic techniques were to be used. The plane of interest is sliced out of the model and inserted as the specimen in Fig. 2.5. A diffraction grating is created as above. Now, if the specimen is annealed, stresses will relax. The specimen will relax accordingly. The interference pattern seen by the observer will represent the negative of the stress-induced displacement. Reduction of this data is more complicated than the 2-D case but is sometimes possible.

Post [53] gives a very readable explanation of holographic interferometry. Dandliker and Ineichen [70] apply this methodology and explain specifics of holographic strain measurement. Dudderar and O'Regan [71] used holographic interferometry to study strain near crack tips. Their work involved the use of a transparent (transmission) specimen, but the principles are equivalent. Dudderar and Gorman [72] used this method to find crack tip stress intensity factors.

X-ray diffraction techniques have developed into a reliable tool for determining residual stresses. These methods also hold promise for more general stress analysis problems. Stress concentration factors are one such possible application.

The basis of x-ray diffraction is the Bragg law. X-rays of wavelength λ are incident on the surface of a polycrystalline material (Fig. 2.6). Bragg's law states that the angle of reflection is related to λ and lattice spacing d, thus:

$$n\lambda = 2\ d\ \sin\theta\ . \tag{2.11}$$

n is the diffraction order of the reflected beam. A change in lattice spacing, d, (under stress) can be used to approximate strain:

$$\varepsilon = \frac{\Delta d}{d} = -\ \cot\ \theta\ \cdot\ \Delta\theta\ . \tag{2.12}$$

A relation for in-plane stress is developed by French and MacDonald [73].

A scenario for measuring elastic stress at the root of a notch follows. A specimen is made from a suitable annealed polycrystalline material (mild steel, for example). Bragg angle, θ, is measured for this unloaded state. Elastic load is applied and Bragg angle checked again. Stress is found from the change in θ and material properties.

A major difficulty in this application is notch root accessibility. The x-ray beam must not strike the specimen normal to the surface. It must make an angle of no less than 15° to the normal. This eliminates many deep notches as candidates for this method.

Thin 2-D specimens can be used as the beam is applied transversely to the specimen load axis. This, however, contributes to error and complicates computations due to dependence on poisson effect.

Several sources are available on the subject. In 1969, French and MacDonald [69] discussed practical aspects of x-ray stress analysis. Their work centers on residual stresses. Rowlands [74] gives a brief outline of the technology. Noyan and Cohen [75] present detailed work

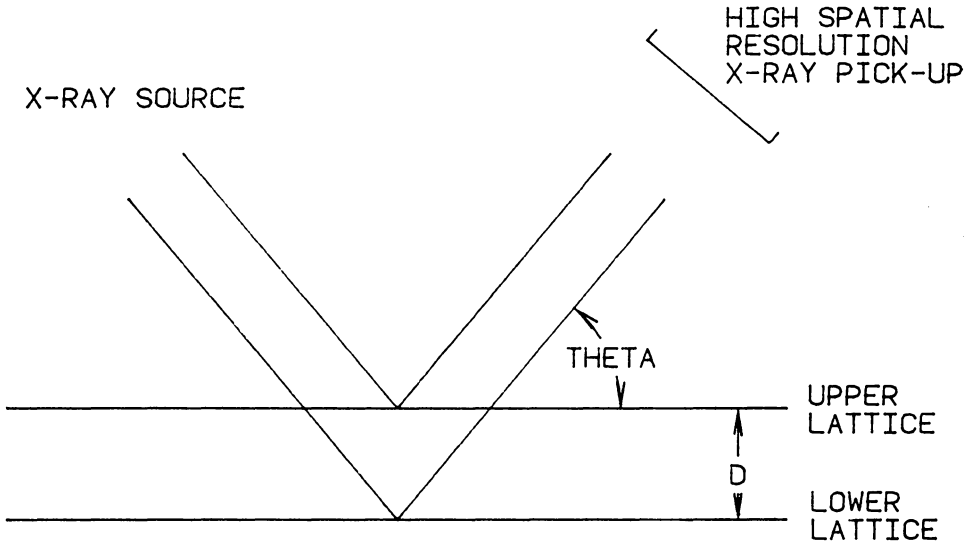

FIGURE 2.6 BRAGG DIFFRACTION

developing and applying the method as well as analyzing results.

Finally, two other possible methods of SCF determination should be mentioned. The first is acoustic emission. When materials undergo deformation or fracture, acoustic waves are produced. These sub-audible, transient strain waves can be measured. By correlating known material/strain data with their acoustic emission outputs, a useful method can be developed. It is conceivable that this method could be used to find SCF's. Much work must first be done to allow practical utilization of this technique.

Similarly, exo-electron emission is a fledgling experimental method. Deformation of certain materials stimulates emission of surface electrons. Correlation of emission and strain data would allow for practical quantitative work. Again, this method needs much work to make it a useful experimental method.

CHAPTER 3
BRITTLE SPECIMEN FAILURE

As part of a classified project, it was necessary to determine the stress concentration factors (SCF's) for 8 specimen geometries. The geometries, shown in Figs. A-1 through A-8 of Appendix A, exhibit a variety of notches and combinations of notches. These combinations include opposed U notches, opposed V notches and U opposite V notched specimens. The method of strain gaging (Chapter 7) was used to determine the SCF's. This work was done to verify complimentary finite element work (Kosmatka et al. [76]). Both sets of results are shown in Table A-1.

As stated in Chapter 2, there are many experimental methods available for SCF work. This thesis compares five of these methods. To do so, specimen geometry A-5 (Fig. A-5 and Fig. 3.1) was chosen for comparitive testing. In addition to strain gage work, SCF's were determined using brittle failure, photoelasticity, and Moire interferometry. Additionally, brittle coating SCF determination was attempted for the geometry of Fig. 4.1. Using the knowledge gained during, and results of, these tests, the methods are compared.

In this thesis, a stress concentration factor is defined the following way. It is the maximum stress occurring in a notch root divided by the nominal stress occurring in the minimum specimen cross sectional area. This minimum area will, henceforth, be referred to as the throat area. Nominal stress for axial SCF's is found

$$\sigma_{nom} = \frac{P}{A_t} \tag{3.1}$$

where P is load and A_t is the throat area. For bending, nominal stress

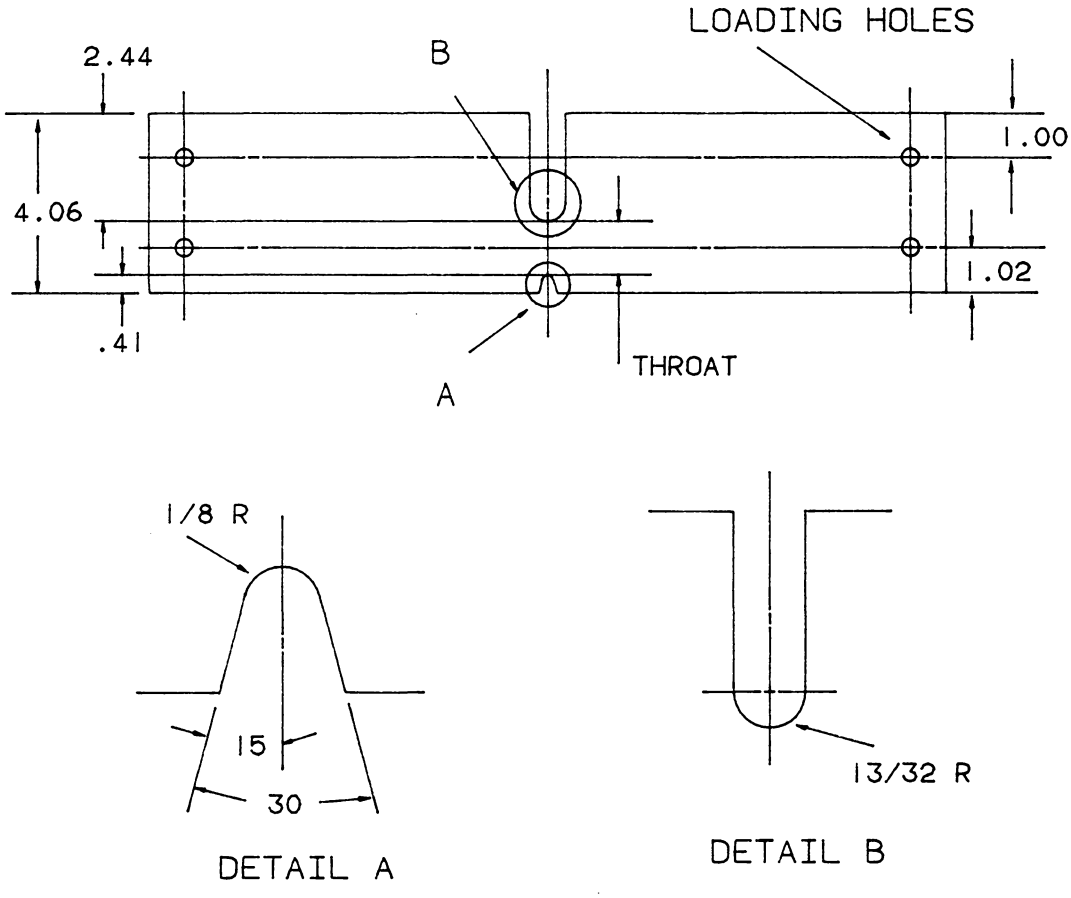

FIGURE 3.1 TEST PIECE GEOMETRY

is defined as

$$\sigma = \frac{Mc}{I} \tag{3.2}$$

where I (moment of inertia) is found for the throat area.

Pure axial load was applied to gather data for axial SCF's (K_T). Because of the difficulty involved in applying pure moment, a combination of axial load and bending revealed bending data. The axial component was removed using analytical techniques explained in Chapters 6 and 7.

The first step in the brittle failure technique is material choice. Options include glasses, ceramics, cast irons, brittle plastics, and carbons/graphites. Glass is not recommended because of its variable strength as discussed in Chapter 2. Machining of glass is also difficult. A large data base along with statistical analysis could probably produce accurate results. However, testing this many specimens would be expensive and time-consuming, rendering glass impractical.

Success has been reported by several authors using PMMA (plexiglass) and graphite. Cast iron was chosen for this test due to its availability and machinability.

Two notched specimens were machined according to Fig. 3.1. A tensile calibration specimen was machined from the same sheet of iron, with load axis parallel to those of the notched specimens. Clamps were used to affix each specimen in a hydraulic tensile machine. Care was taken to assure the specimens were axially loaded. Failure of the calibration specimen revealed the iron to have a tensile strength of 4780 psi (32.96 MPa). Each of the two notched specimens were then pulled to failure.

Notched specimen number 1 failed at 780 pounds (3470 N) of load. The failure was observed to initiate on the V side (as expected), at the root of the notch. However, the stress in the throat at the time of failure was nearly exactly the strength found above. The "SCF" was found to be 1.02.

The second notched specimen was loaded as described above. Failure occured at 540 pounds (2402 N). However, the crack initiated near the notch root of the U side. All available information indicates that the V-side SCF is greater. This would mean that failure should initiate at the V-root. If the available information is to be believed, the experimental result should be explained. It is apparent that the specimen was not affected by the small radius on the V-notch root. The critical stress riser is then something undetected in the region. This riser is probably a microscopic imperfection in the iron surface. Creyke [78] suggests that carbon flakes cause such stress risers on the surface of cast iron.

It is also interesting that specimen 1 failed when its nominal stress was equal to the strength of the calibration specimen. This also hints that the highest SCF was due to a microscopic flaw and not due to the V notch.

This testing revealed several things. Primarily, it indicates that cast iron is not promising for brittle failure work. It did, however, show the testing to be quick and simple to perform. Inexpensive plaster-of-paris or PMMA holds promise for such work. Use of plaster-of-paris would minimize machine time. Once a mold were created, many specimens could be formed. This method is only recommended for simple 2-D geometries.

CHAPTER 4
BRITTLE COATING

Brittle coating methods can be applied to 3-D parts having complex geometries. To satisfy test requirements and to gain confidence in the method, a number of 2-D specimens were machined from aluminum in the shape given in Fig. 4.1. As described in Chapter 2, the groove region is coated with brittle lacquer. The specimens are then given incremental axial load until the brittle coating cracks at the notch root. Coated calibration bars are used to determine failure strain. Root stress can then be found.

Commercially available brittle lacquer (Stresscoat®) was purchased. The liquid was applied to each batch of specimens and calibration bars simultaneously. Application was done using a binks-type spray gun using compressed nitrogen. A test batch typically consisted of 4 notched specimens and 4 calibration bars. Batches were allowed to dry overnight.

An Instron tensile machine was fitted with grips to hold the specimens. The machine was set to the slowest strain rate. Specimens were affixed in the grips. Strain was applied as the well-lit groove was observed through a magnifying lens. As the first crack appeared, tensile load was recorded.

The calibration bars were then used to find the strain, ε, necessary for coating failure. Knowing this and Youngs Modulus, E, the root stress at cracking load, P, is given by

$$\sigma = E \varepsilon \ . \qquad (4.1)$$

The stress concentration factor is thus

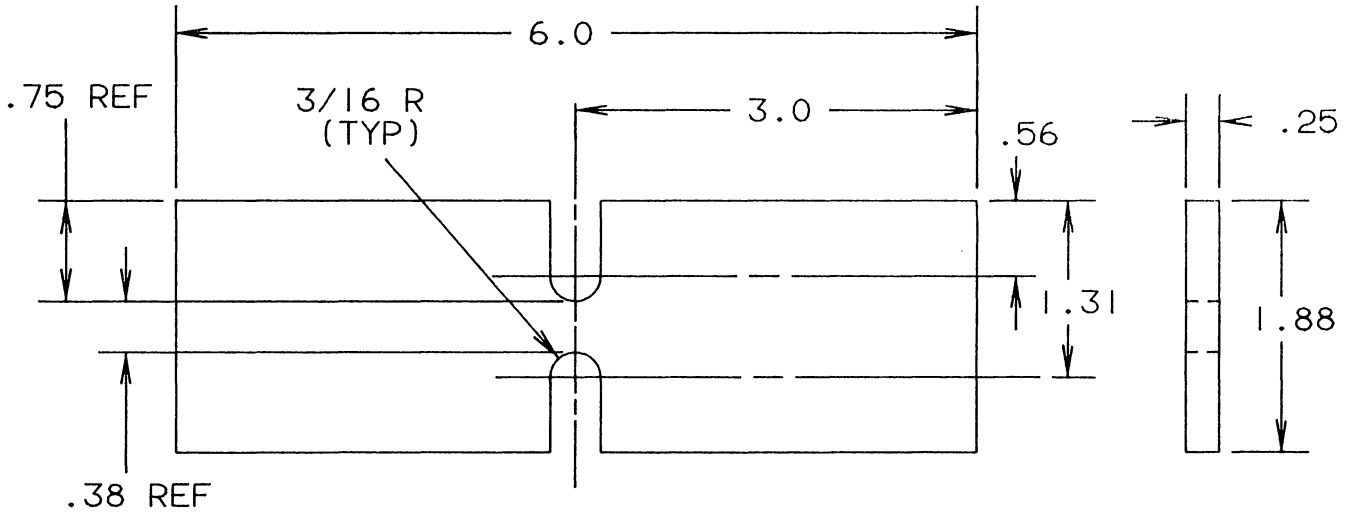

FIGURE 4.1 BRITTLE COATING TEST SPECIMEN

$$K = \frac{\sigma}{(P/A)} \tag{4.2}$$

where A is the minimum specimen throat area.

The results are not encouraging. Table 4.1 (Samples 1-11) shows the results of this testing.

In an attempt to improve the poor results, a fourth batch was coated as above. The coated specimens were then held at 80°F (27°C) for 12 hours to minimize effects of coating thickness variation. This procedure is recommended by the manufacturer. Testing was carried out as above, but the magnifying glass was replaced by a boroscope. This device helped maintain a very close watch for first cracks.

Table 4.1 shows the results to be not better for these final 3 specimens. All SCF values are obviously wrong, being less than 1.

The Literature Review in Chapter 2 shows that this method has been carried on with success in the past. New EPA regulations have recently forced a change in lacquer formula. This change is perhaps responsible for the inconsistency and scatter of data obtained here. Another possible source of error lies in the observation of the first crack.

It was difficult to see the hairline cracks in the coating. The boroscope aided this process but results failed to improve significantly. Perhaps a black anodized specimen surface would improve the problem. It is thought, however, that the majority of error is due to poor coating performance.

Table 4.1 Brittle Coating Test Results for a Published Stress Concentration Factor of a Double "U"-Notch at K_T = 1.68*

Sample	Cracking Load lb (N)	Calibration Bar Crack Initiation Strain (μin/in or μm/m)	Stress Concentration Factor
1	4350 (19351)	410	0.09
2	700 (3114)	410	0.556
3	950 (4226)	410	0.41
4	1000 (4448)	410	0.39
5	3600 (16014)	625	0.16
6	4200 (18683)	625	0.14
7	3650 (16237)	625	0.16
8	did not fail	625	--
9	did not fail	500	--
10	4200 (18683)	500	0.11
11	1900 (8452)	500	0.25
12	530 (2358)	515	0.92
13	1850 (8230)	515	0.26
14	1900 (8452)	515	0.26

* As given by Haywood

CHAPTER 5
MOIRE INTERFEROMETRY

Moire interferometry is a powerful experimental method. It is a sensitive, high resolution means for determining in-plane displacements. As described in Chapter 2, using digitization, strains, and thereby stresses, can be found.

A Moire test was run on the (standard) geometry specimen of Fig. 3.1. The first objective was to determine stress concentration factors. In addition, the high resolution of this method offers guidance for strain gage selection (Chapter 7). Gages simply average the strain over the gage length. With the Moire test, it is possible to approximately measure the length over which the maximum stress occurs. This information is valuable in strain gage selection.

Chapter 2 showed each displacement fringe of this method to be inverse of the reference grating frequency. The following test was run with a reference grating of 2400 lines/mm.

Moire interferometry was explained briefly in Chapter 2. This explanation involved the use of 2 real, transmission-type gratings. The following test was run with a reflective type specimen grating. It works on the same principles as outlined for transmission gratings.

Figure 2.2 shows the results of two intersecting coherent beams. Equation (2.5) gives the frequency, f, of this pattern in terms of intersection angle and wavelength. This pattern is equivalent to a real grating of frequency, f. A virtual grating such as this can be used for the reference grating.

In order to perform the test, a proper specimen had to be

created. Two-dimensional Moire is began by replicating a 1200 line-per-millimeter reflective grating on the face of the chosen specimen (Fig. 3.1). As the specimen is strained, the grating strains with it. As explained in Chapter 2, the data from Moire originates from the change in grating frequency.

First, a grating mold had to be created. Two beams of coherent light were crossed as in Fig. 2.2. The angle between them was adjusted so that (from Eq. 2.5) the frequency of interference was 1200 lines/mm. A high resolution photographic plate was exposed in plane A-A of Fig. 2.2. When the plate was processed, silver compounds in the exposed region were washed away, leaving a corrugated grating of 1200 lines/mm. This mold had to be coated with silver for transfer to the specimen. Silver was evaporated onto the surface in a closed container using a high-temperature tungsten filament.

The grating now had to be replicated on the specimen surface. A puddle of epoxy was put on the specimen. Using optical alignment techniques, the silvered corrugated surface was carefully pressed onto the adhesive. Pressure was maintained overnight. The mold was then lifted from the specimen, leaving the desired reflective grating. Quality of this particular replication was quite good.

Loading was to be applied along the axis of notch symmetry only. This would reveal axial stress concentration factors. A loading frame was mounted to the optical table. The specimen was hung vertically in the frame. A horizontal reference grating of 2400 lines per millimeter illuminated the horizontal specimen grating. Such an arrangement reveals vertical (Y) displacement. The no load field was photographed.

This is shown in Fig. 5.1. The reference grating was then rotated to reveal horizontal (X) displacements. This photograph is shown in Fig. 5.2.

Load was applied in 100 pound (444.8 N) increments. It was planned to load to 800 lbs (3559 N), within 5% of the expected yield load of 840 (3737 N). As a precaution against specimen destruction, each Y displacement field was photographed at 100 pound (444.8 N) increments. 800 pounds (3559 N) was successfully reached without yield. Yielding would have damaged the specimen grating, which is easily noted upon return to zero load. The X and Y fields at this load are shown in Figs. 5.3 and 5.4.

The raw data was now in the form of vertical displacement contour photographs.

With this displacement data in hand, useful strain information had to be derived. Primary to this operation is the familiar relation

$$\varepsilon_{yy} = \frac{\partial U_y}{\partial y} \tag{5.1}$$

which for this finite difference data can be approximated

$$\varepsilon_{yy} = \frac{\partial U_y}{\partial y} \doteq \frac{\Delta U_y}{\Delta y} . \tag{5.2}$$

Now U_y is defined by the Moire interferometric relation

$$U_y = \frac{\Delta N}{f} \tag{5.3}$$

where N is the fringe order and f is the reference grating frequency. Best accuracy is attained if ΔN is 1 (as opposed to 2 or 3). For

Fig. 5.1 No-Load Vertical (Y) Displacement Field

Fig. 5.2 No-Load Horizontal (X) Displacement Field

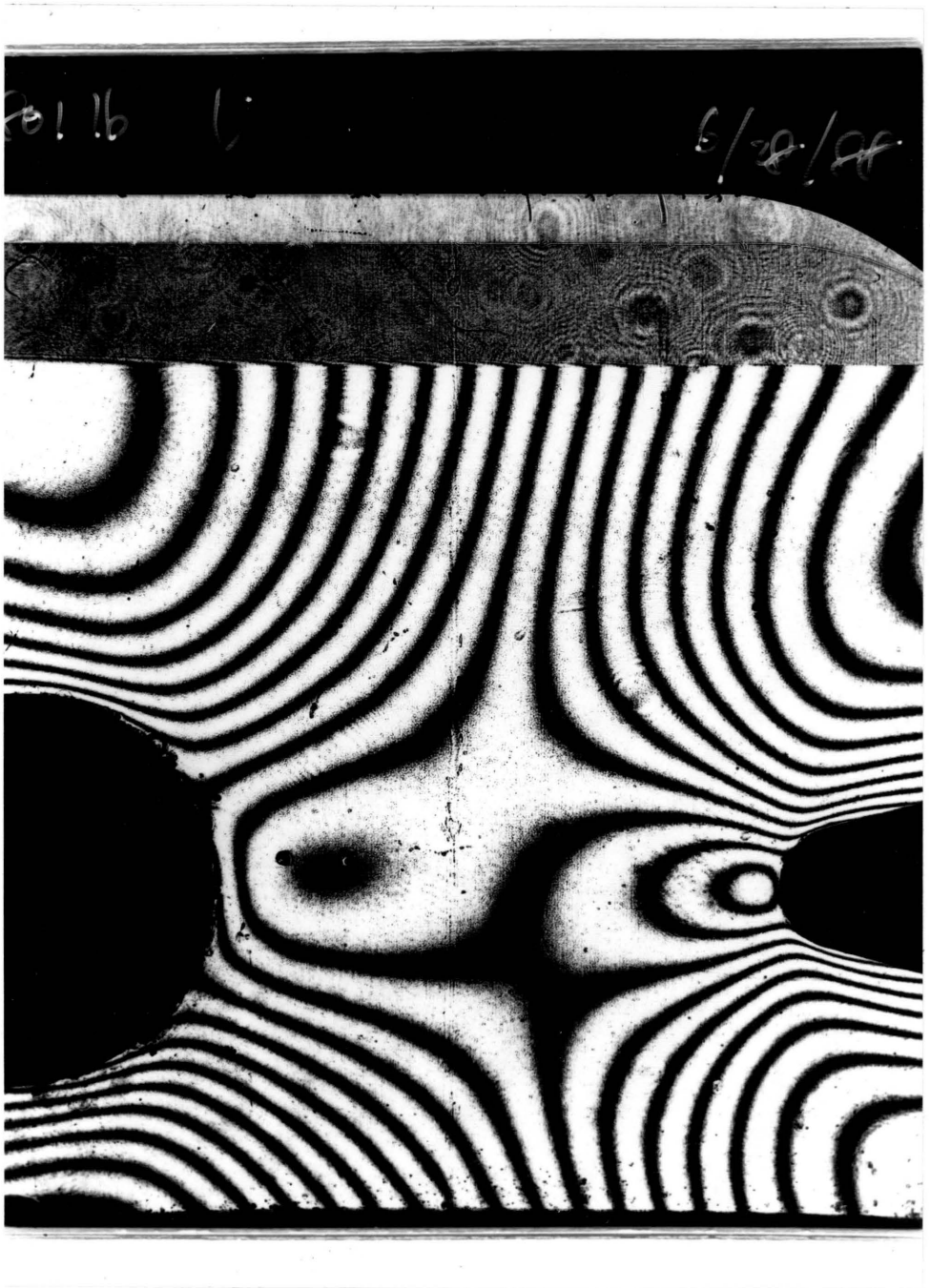

Fig. 5.3 Horizontal (X) Displacement Field at 800 Pounds (3559 N)

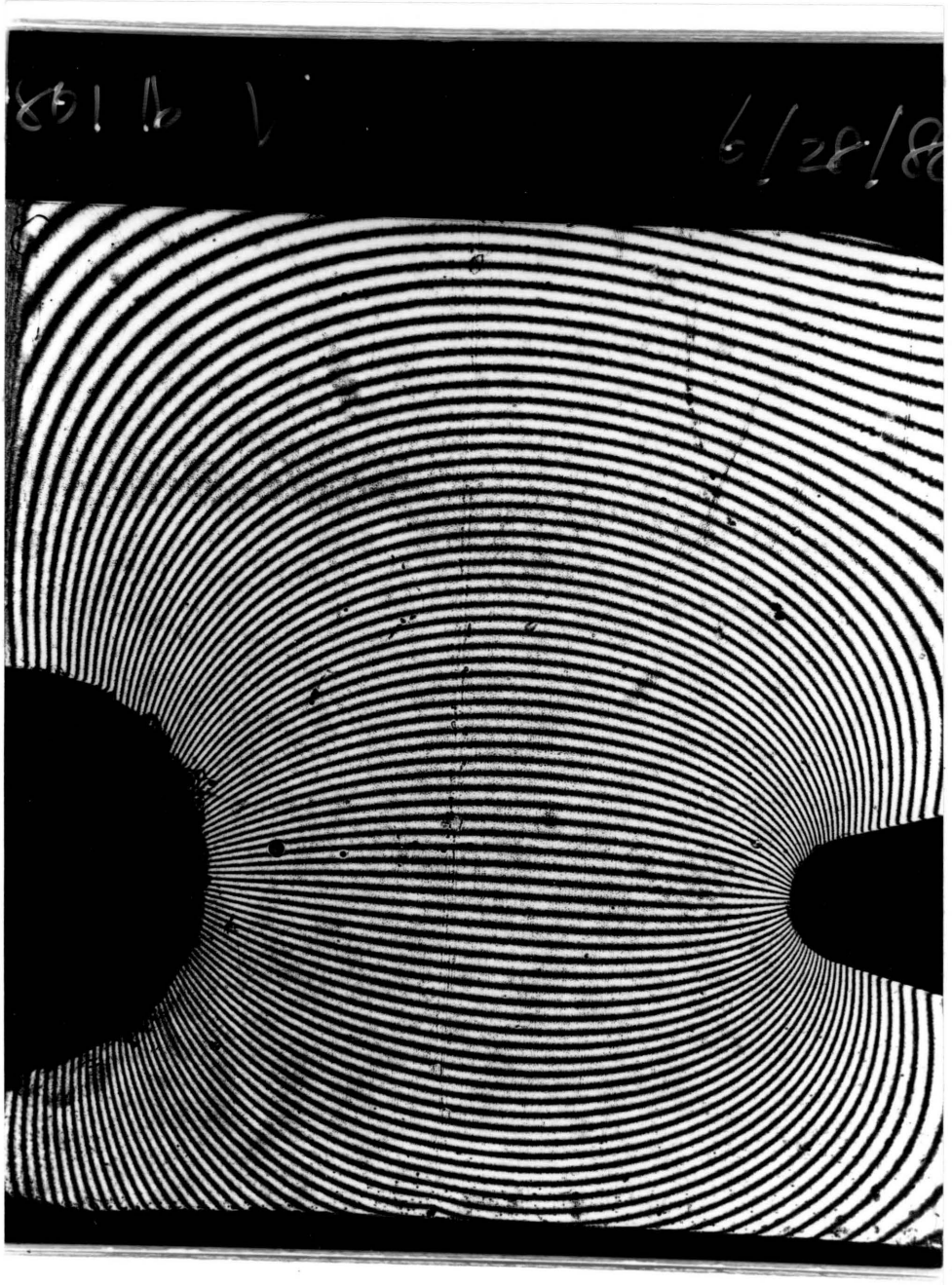

Fig. 5.4 Vertical (Y) Displacement Field at 800 Pounds (3559 N)

this, Δ y (Eq. 5.2) is the distance between a change in fringe order of 1.

Photographic enlargement to 8 times actual specimen size and a sensitive digitizer gave resolution to 0.0001 in (.000254 cm) for Δy determination. Distance between fringes was determined at and near the notch root for both U and V notches. This "digitization" process was carried out four times in an attempt to minimize errors. Strain was then approximated using this data and Eq. (5.3). Approximate stress was then calculated using Hookes law. Nominal stress was calculated by dividing the tensile load by the throat area.

Table 5.1 shows the stress concentration factors along the notch bases. The highest SCF for the U-notch is shown to be 2.43. The highest SCF found on the V side is shown as 3.03. Figures 5.5 and 5.6 are graphs of K_T vs. distance from notch root for each notch.

The stress concentration factor found on the V side matches almost exactly the experimental results of equivalent strain gage work (Chapter 7). Figure 5.4 shows the displacement pattern (lines of constant displacement) at the V root to be clear and well defined. This clarity is the reason for such good test results.

Deflection data from the U-groove region is not as clear or well defined. A residual layer of photo-resist (used in grating replication) clouds the region. The specimen was cleaned and retested, but to no avail. From the onset of digitization, it was realized that this would affect results. Figure 5.5 particularly shows the resultant noise. Apparent SCF's vary, up and down, from 1.93 to 2.43 near the notch root. The obviousness of the clouded data is an advantage of Moire

Table 5.1 SCF Distribution

U Notch

Distance from Notch Root in (cm)		K_T
0.0336	(0.0853)	2.15
0.0283	(0.0719)	2.04
0.0230	(0.0584)	2.19
0.0180	(0.0457)	2.28
0.0129	(0.0328)	2.15
0.0079	(0.0201)	2.28
0.0027	(0.0069)	2.07
0	(0)	--
0.0029	(0.0074)	1.93
0.0085	(0.0216)	2.11
0.0134	(0.0340)	2.43
0.0182	(0.0462)	2.28
0.0233	(0.0592)	2.11
0.0286	(0.0726)	2.11
0.0339	(0.0861)	2.07

V Notch

0	(0)	--
0.0019	(0.0048)	3.03
0.0057	(0.0145)	2.80
0.0097	(0.0246)	2.87
0.0136	(0.0345)	2.80
0.0175	(0.0445)	3.03

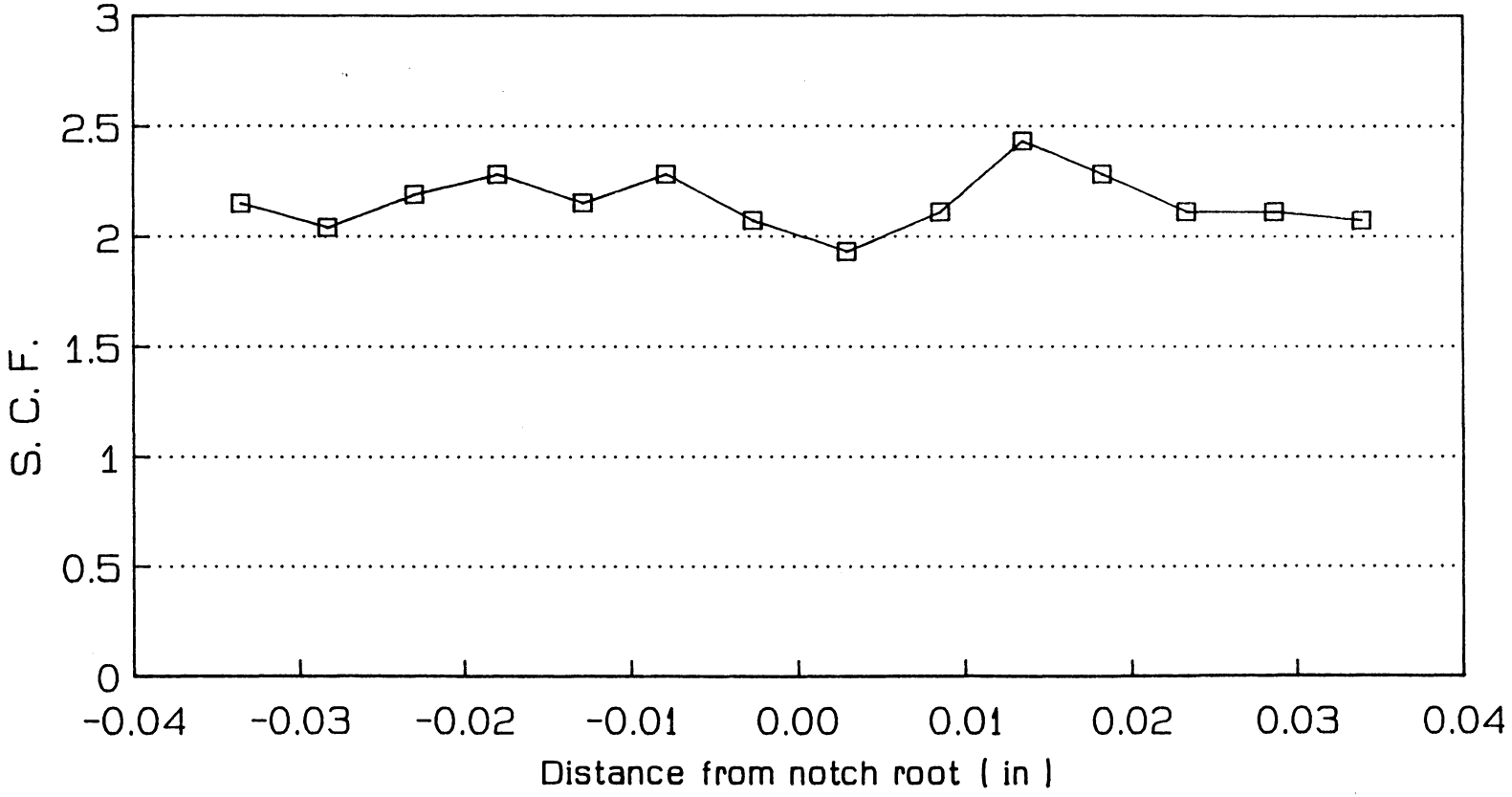
S.C.F. Distribution
(U notch)
S.C.F.
3
2.5
2
1.5
1
0.5
0
-0.04
-0.03
-0.02
-0.01
0.00
0.01
0.02
0.03
0.04
Distance from notch root (in)

Fig. 5.5

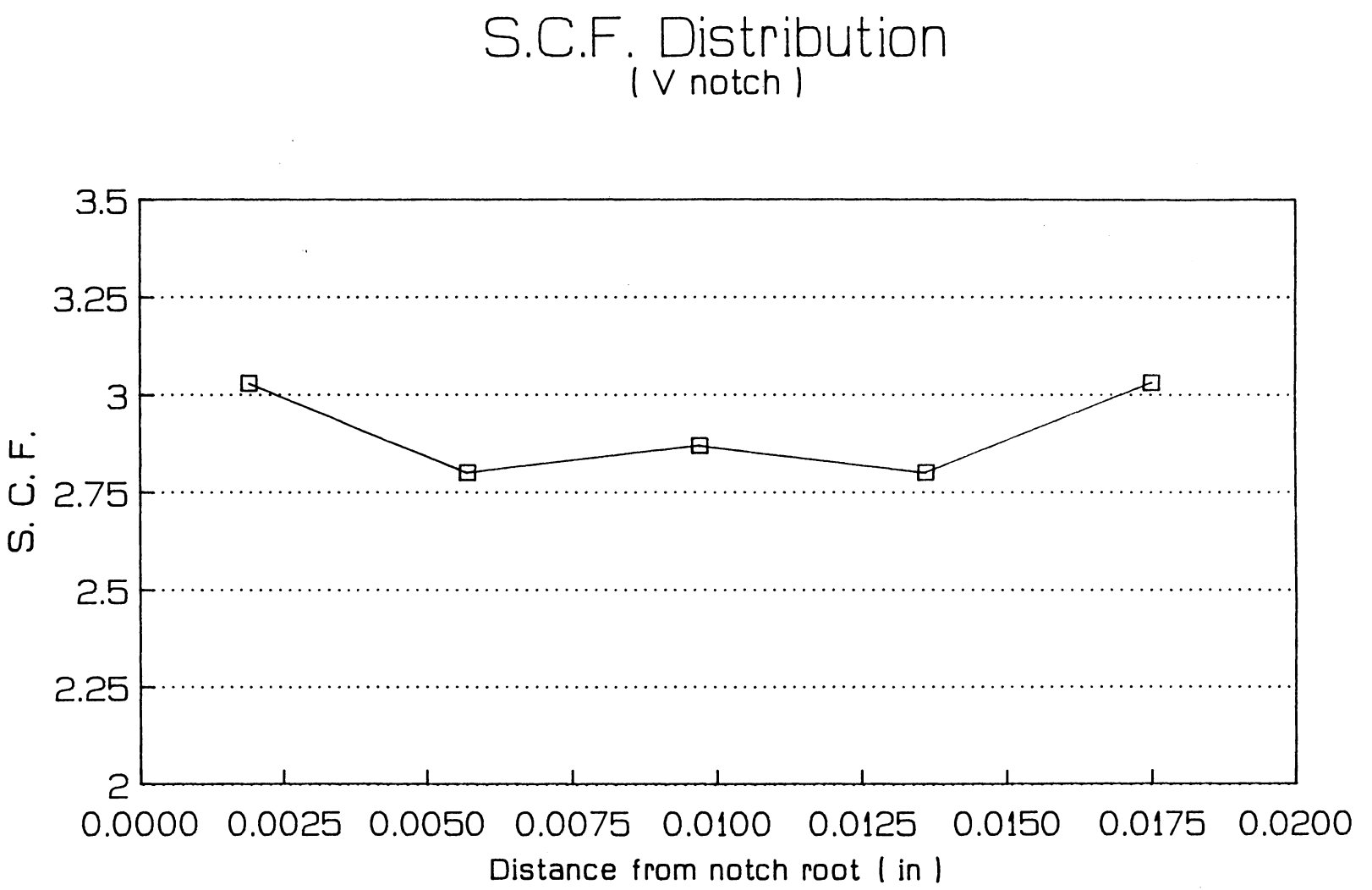
S.C.F. Distribution
(V notch)
3.5
3.25
3
2.75
2.5
2.25
2
S. C. F.
0.0000
0.0025
0.0050
0.0075
0.0100
0.0125
0.0150
0.0175
0.0200
Distance from notch root (in)

Fig. 5.6

interferometry. An untrained eye can readily spot regions of poor resolution. Data from this region can then be treated with caution. The reader should observe (Fig. 5.4) that the entire grating is clear and readable in a great majority of locations.

Smooth and clear Moire stress contours, such as Fig. 5.6, can be of great assistance to other stress analyses. Such a contour can be used to help choose strain gage sizes for related work. Such an application will be made in Chapter 7.

CHAPTER 6
PHOTOELASTICITY

A 2-D photoelastic test was performed to investigate the SCF's of the notch geometry in Fig. 3.1. This chapter documents this testing.

First, the specimen had to be thin enough to avoid 3-D effects. Excessive specimen thickness would cause ε_3 to be significant. A thickness of 0.233 in (0.592 cm) was chosen. A commercial photoelastic material (PSM-1) produced by Measurements Group was picked for its low fringe constant. This means it produces many fringes per unit load and thus gives good resolution. This fringe value is 40 psi/fringe/inch (700532 MPa/fring cm) as determined by the manufacturer.

The specimen was machined according to Fig. 3.1. Small load holes are adequate for inducing moment. This is because bearing stress is not critical at the holes when compared to bending stress in the throat region. For axial load, however, the load holes had to be enlarged to prevent bearing failure at loads necessary to produce enough fringes in the throat.

A polariscope, like the line in Fig. 2.1, was used. A mercury vapor lamp supplied necessary monochromatic light. The specimen was hung vertically from U-joints through its moment load holes. The U-joint served to minimize any unintentional bending moment. Weight was slowly added to the lower moment point. Meanwhile, position of the zero order fringe (blank fringe occupying region of interest at no load) was monitored. At 18.5 pounds (82.3 N), a sufficient number of fringes existed near the notches and the zero order fringe was still visible. This can be seen in Fig. 6.1. The scratch on the V-side will be

Fig. 6.1 Photoelastic Stress Contour Axial/Bending Load

discussed later in this chapter.

The photograph was taken using Kodak technical-pan 35 mm film. The aperture was set to F-4, and the shutter speed was 1 second. The negatives were developed in Kodak D-19 developer for 7 minutes.

Data reduction was fairly simple. First, fringe order had to be determined at the points of interest. With the zero order fringe in the center, each white fringe was counted to the notch root. The governing equation

$$\sigma_1 - \sigma_2 = \frac{N f}{t} \tag{6.1}$$

was used. N is the counted fringe order (7 on the V side, 6 on the U side), f is the fringe constant (40 psi/fringe/in or 700532 MPA/fringe/cm), and t is the specimen thickness (.233in or .592 cm). σ_2 is known to be zero at the notch root, therefore σ_1 can be found directly.

Axial loading was administered using the same method. In this case, 154 lbs (685 N) was necessary to produce enough fringes. Too few fringes would not allow enough resolution. At this high load, the 1.5 order fringe occupied the throat center. The zero, 1/2, and one order fringe had disappeared during load. This condition can be seen in Fig. 6.2. Fringe orders were counted and stresses found from Eq. (6.1).

Specimen inspection revealed that the axial loading holes were slightly off center. For this reason, data was reduced in the following manner.

For the moment loading, stress (σ_U) was found at the U groove from Eq. (6.1). This was substituted into

$$\sigma_U = K_{T(U)} \frac{P}{A} + K_{B(U)} \frac{M c}{I} , \tag{6.2}$$

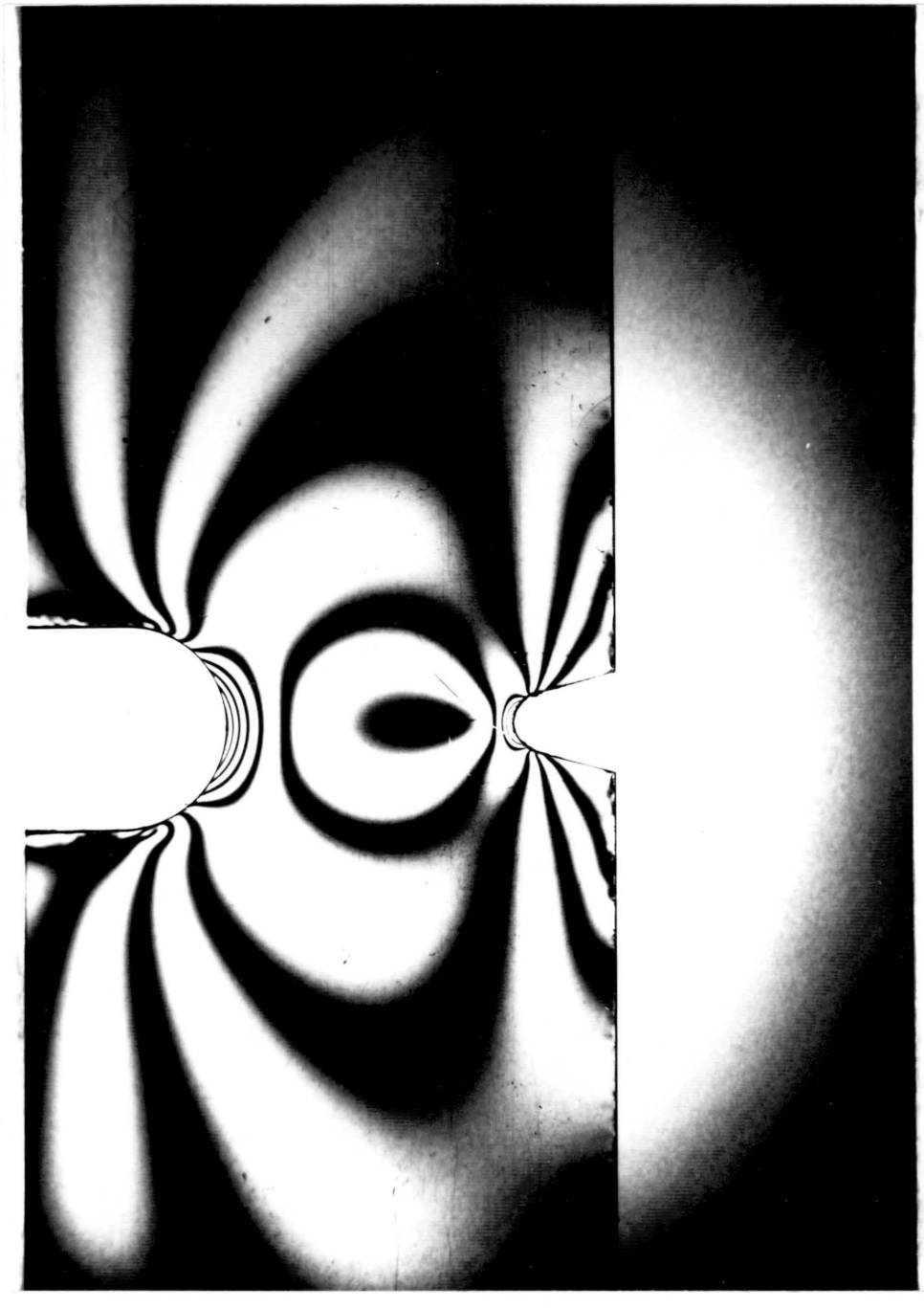

Fig. 6.2 Photoelastic Stress Contour, Pure Axial Load

where P is load, A is throat area, $K_{T(U)}$ is the axial stress concentration factor, M is moment (load x eccentricity), c is the distance from groove to throat centroid, I is the throat moment of inertia, and $K_{B(U)}$ is the bending stress concentration factor. The same was done with the axial loading data for the U side. The two equations were solved for $K_{B(U)}$ and $K_{T(U)}$.

Equivalent reduction was performed for the V side.

The results are as follows:

V side	U side
$K_T = 2.30$	$K_T = 2.04$
$K_B = 1.88$	$K_B = 1.29$

The U-side SCF's appear to be more accurate than those for the V-side (when compared to strain gage and finite element work). (All results are tabulated in Chapter 8, Table 8.1.) This is probably because the resolution at the U groove is much better than at the V side. Burger [45] presents a possible solution. He includes the fringe doubling polariscope developed by Daniel Post. Increasing the load or use of better photographic optics could also minimize this error.

Finally, the care should be taken to avoid scratching of the specimen surface. The flaw seen clearly in Figs. 6.1 and 6.2 is barely discernible on the model. Yet, it disrupts the fringe pattern and makes fringe ordering more difficult. If this scratch had crossed the point of interest, it would have rendered the model useless.

CHAPTER 7
STRAIN GAGES

Chapter 7, Section I - Specimen Design

Electrical resistance strain gages were used to determine stress concentration factors for a total of 8 double-notched geometries. Micro miniature strain gages (.015 in or .038 cm active gage length) were mounted in the roots of the notches (one gage per root). Axial load was applied to determine the axial SCF. Combined axial and bending load was used to determine the bending SCF.

Root stresses were to be found by multiplying the root strain (found from the strain gages) by Young's modulus for the specimen. For this reason, a test was run to accurately determine Young's modulus. A long rectangular bar was fabricated from aluminum stock. Near the middle, 2 strain gages were mounted. The cross-sectional area of the specimen was determined from geometry. Known axial load was applied to induce about 150 $\mu\varepsilon$. Young's modulus for the specimen material was found from

$$E = \frac{\sigma}{\varepsilon} \tag{7.1}$$

where σ is the known stress (from $\sigma = \frac{P}{A}$) and ε is the experimental strain.

Test specimens were machined according to Figs. A-1 through A-8. Pure axial loading could be easily applied to determine the axial SCF as described in the following sections. Pure bending moment is not as simple to apply. For this reason, tension loads were applied at the "moment" holes. This created a combined axial and bending condition at the notch roots. The effects of the axial component can be

mathematically removed (see Section IV, Data Reduction), leaving a bending stress concentration factor.

Chapter 7, Section II - Gage Selection

The point of maximum stress (strain) in a geometric incongruity is very small in size. Adjacent to this point, stress (strain) falls off, approaching the nominal stress (strain) some distance away. If too large a gage is used, the area averaged strain under the gage is far below the peak strain. If this occurs, the apparent SCF is too low.

This makes gage size selection a critical process. Dr. R. H. Fries [77] analyzed this problem using previously performed finite element analysis [76]. The FEA work involved stresses around the circumference of the radius at a V-notch root. By analyzing the stress distribution, Fries found that a gage length of 1/3 the root radius would result in an error of less than 2%. This magnitude of error is quite acceptable for most purposes and can be improved as notch radius increases for a given gage length.

Commercially available gages with active length of .015 in (.038 cm) were procured. The above analysis shows that proper placement of such a gage would produce good results in roots with very small radii.

The Moire interferometric analysis reported in Chapter 5 can be used for similar error analysis. The root radius for the V notch of Table 5.1 (V) is .0625 in (.159 cm). A measuring length of 1/3 this is .021 in (.053 cm). The data taken in the test covers a region along the notch of about this length. Average SCF in this region is 2.91, nearly 4% low (when compared to the peak SCF of 3.03). This, however, is

acceptably accurate and thus reveals a similar result to the work of Fries.

Chapter 7, Section III - Experimental Method

A recommended epoxy cement (Micro-Measurements® type AE-10) was purchased from the gage manufacturer. This was used to mount the strain gages. Also, portable strain indicators (model P-3500), from the same source, were acquired. These were used to instrument the gages.

The idea behind the testing (axial SCF) was simple. A known weight was hung from the axial load point on the specimen. Strain readings were taken and recorded for later reduction. This section explains the details of the testing procedure.

First, it was necessary to choose the proper loading for each specimen. Loads had to be substantial enough to induce enough strain to negate noise or flutter in the data. However, the weight was to be light enough as not to yield the specimen nor to inconvenience the experimenter. It was decided that readings on the order of 150 micro strain would be sufficient to neutralize noise. Calculations showed that, depending on specimen geometry, this level of strain would be induced by loads ranging from 50 to 200 pounds (222 N to 890 N). Computations were made to ensure that the induced stress would be well below the yield point of the specimens. Two weights of 50 pounds (222 N) each were acquired. One weight of 146 pounds (649 N) and one weight of 196 pounds (872 N) was fabricated.

A block and tackle was built to lift the weights. Figure 7.1 shows a schematic of the specimen loading apparatus. 1/2 in (1.27 cm) nylon

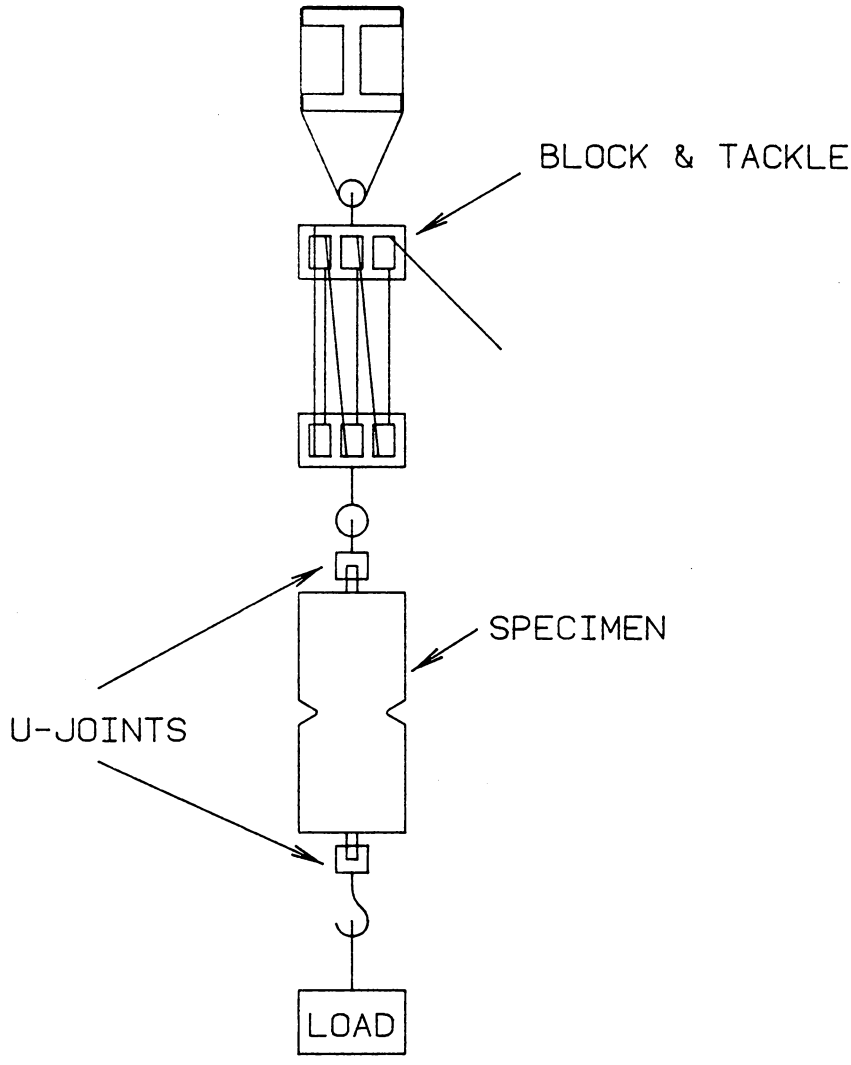

FIGURE 7.1 LOADING APPARATUS

rope tied in a bowline affixes the upper pulleys to the I-beam. 3/8 in (.953 cm) nylon rope was used for the active line. 1/2 in (1.27 cm) nylon was again used to connect the lower pulleys to the upper universal joint as well as the lower U-joint to the weight.

The universal joints were added to ensure that no moment was applied due to uneven loading. This would result from excess friction at the specimen loading interface. The joints were made from mild steel with 3/16 in (.476 cm) hardened steel pins.

Pure axial loading was carried out first. The U-joints were attached to either end of the test piece at the axial load points. The desired load was then attached to the lower U-joint. Strain was induced by raising and lowering the load, thus cyclically loading the specimen. This was done to exercise the gages and minimize zero drift. Each specimen was exposed to 10 or so loading cycles.

The strain indicators were zeroed and the load was hoisted. The strain reading for all instrumented gages was recorded. The specimen was unloaded and a final "zero" strain was recorded. This final reading usually ranged from -5 $\mu\varepsilon$ to +5 $\mu\varepsilon$. This "zero drift" was accounted for in the reduction of data. The indicators were again zeroed and the test was repeated. A total of 3 load tests were run.

The above procedure was repeated for loads attached at the moment inducing load points. The resulting data was then reduced to determine the bending SCF.

Chapter 7, Section IV - Data Reduction

Axial SCF

In Chapter 1, SCF was defined as the ratio of local stress to the average stress in the throat region. That is

$$K = \frac{\sigma_{local}}{\sigma_{avg}} . \tag{7.2}$$

The value of $\sigma_{nominal}$ was determined using the simple relation

$$\sigma_{nominal} = \frac{P}{A_{throat}} \tag{7.3}$$

where P is the applied load and A_{throat} is the minimum throat area. The local stress, σ_{local}, was determined using the relationship

$$\sigma_{local} = E\, \varepsilon_A . \tag{7.4}$$

In this expression, E is the experimentally determined modulus of elasticity for the specimen material. The value of ε_A was found, thus

$$\varepsilon_A = \frac{\sum_{i=1}^{3} \varepsilon_i - \sum_{i=1}^{3} Z_{fi}}{3} . \tag{7.5}$$

ε_i is the recorded strain under load while Z_f is the final "zero" reading after the load is removed.

A computer program was used to carry out the above data reduction. This program is listed in Appendix B.

Bending SCF

A combined bending/axial loading was used to derive data for the bending SCF's (K_B). This loading method was discussed in the section on specimen design. It is now necessary to explain how bending SCF's were obtained from this loading method.

Take, for example, a typical specimen of Fig. 7.2. The stress at point B is represented by

$$\sigma_B = K_B \frac{M\,c}{I} + K_T \frac{P}{A_{throat}}$$

$$= K_B \frac{P\,E\,c}{t\,(2c)^3\,(1/12)} + K_T \frac{P}{A_{throat}}$$

$$= \frac{3}{2} \frac{P\,E}{t\,c^2} K_B + \frac{P}{A_{throat}} K_T \qquad (7.6)$$

where P is load, E is eccentricity, t is specimen thickness, A_{throat} is throat area, and c is the distance from B to the throat centroid. K_T was determined experimentally from true axial loading, as described in the above discussion. The stress at B is also known to be the measured strain multiplied by the specimen Young's modulus. Therefore, K_B can be solved for directly since all the remaining variables are known from geometry and loading.

$$K_B = \left(\sigma_B - \frac{P}{A_{throat}} K_T\right) \frac{2}{3} \frac{t\,c^2}{P\,E} \qquad (7.7)$$

A computer program listed in Appendix B carries out this calculation.

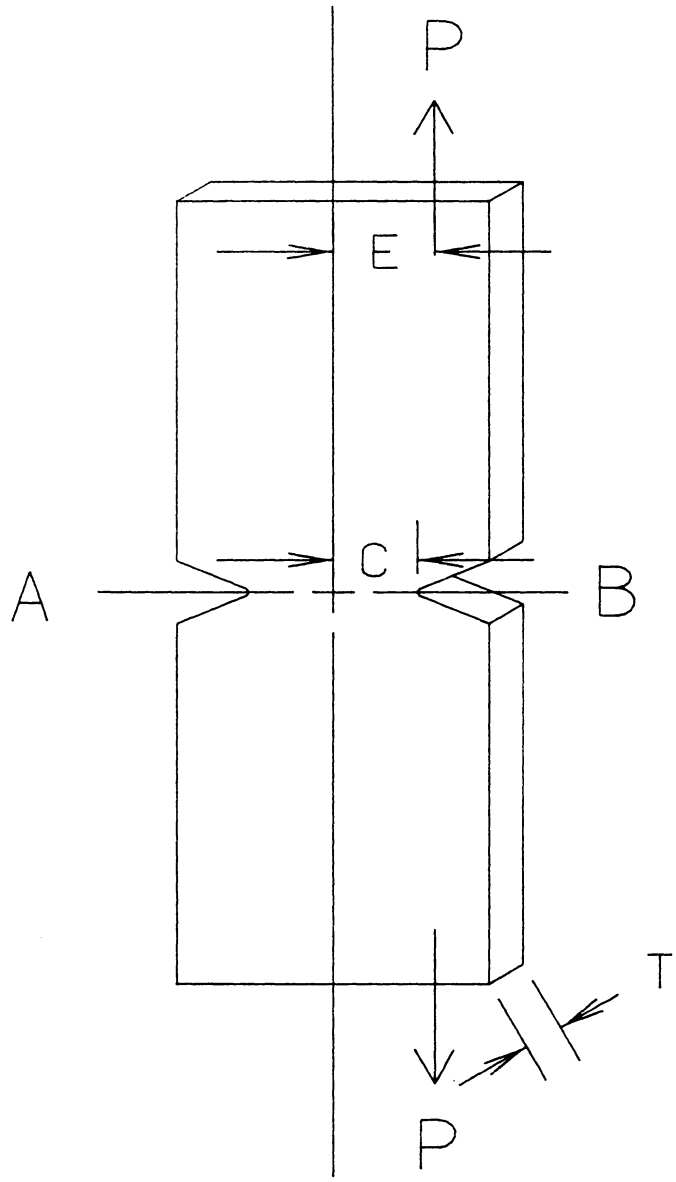

Fig. 7.2 Data Reduction Geometry

CHAPTER 8
COMPARISON OF RESULTS

By testing the same geometry using different experimental methods, the methods themselves could be compared. The common ground used for comparison in this thesis are stress concentration factors.

Kosmatka et al. [76] performed finite element analysis on the geometry of interest. This work produced axial stress concentration factors. Their results will also be compared to the experimental results.

Ideally, a theory of elasticity solution would be available as another yardstick. However, because of the relatively complex geometry of the test piece, no such solution is available. For use as a comparative tool only, Fries and Biegler [78] approximated SCF's for the U and V notches. This was done by creating a symmetric double U-notch specimen and a double V-notch specimen with throat width equal to the specimen of interest (Fig. 3.1). Each created geometry was then analyzed by theory of elasticity solutions. The U notches were equivalent to the U notch of Fig. 3.1. The V notches were equivalent to the V notch of Fig. 3.1.

Table 8.1 shows experimental results, finite element results, and the theory of elasticity approximations for SCF's for the common test piece.

Strain Gage

The axial U-notch (SCF) result from the strain gage testing precisely matches the finite element results. Additionally, both values (K_T and K_B) are nearly equal to the theory of elasticity estimate.

Table 8.1 Comparison of Results

	V		U	
	K_T	K_B	K_T	K_B
Strain Gage	2.98	2.29	1.92	1.40
Photoelasticity	2.30	1.88	2.04	1.29
Moire	3.03	*	2.43	*
FEA	2.52	*	1.93	*
Elasticity Estimate	2.9	**	1.9	1.5
Brittle Specimen	1.02	*	***	***

*Bending case not investigated.

**Solution not available.

***V side data only from brittle failure.

Because of this, confidence is high that both K_T and K_B found for the U groove by strain gages are correct. Additionally, the elasticity estimate for K_B reinforces this conclusion.

For the V side, the strain gage K_T exceeds the FEA result by about 15%. The elasticity estimate indicates that the true K_T might lie between the two values.

Among the experimental methods, strain gaging emerged as a reliable analysis tool. Its concepts are simple to understand. Although it is not a full-field method, it was very useful for determining SCF's at a known point of interest. One potential problem is that the location of stress concentrations must be precisely known before testing. Gaging is not recommended for developing stress contour fields. Fortunately, stress risers are usually easily observed by a well trained engineer. This is because stress risers usually occur at changes in geometry. For this reason, strain gages are highly recommended for stress concentration work.

Photoelasticity

Photoelasticity methods have been used for a great while in SCF studies. U-groove SCF results can be seen to closely match (5%) finite element results. The V side K_T is also reasonably close (10%) to FEA values. Methods are available to increase resolution of photoelastic data. Had these been employed in the testing, discrepancies would likely have been less. The fact that the most basic photoelastic analysis can produce results as good as these shows how powerful a method this is.

Photoelastic techniques are easily learned and the theory is quite understandable. The method is old enough that there exists a great volume of information on the subject. Further, many persons are well-versed in the method. This in itself is an asset to the technique.

The greatest drawback of the method seems to be initial cost. This, however, is minimal when compared to x-ray method or S.P.A.T.E.® technology. Another drawback is the susceptibility of the plastic specimens to surface damage. A scratch, like that seen in Fig. 6.1, can render a specimen useless. Care must be taken to protect specimens from damage.

Photoelastic models are easily and cheaply machined. Further, the data they produce is easily reduced form photograph form. Photoelasticity is a full field method. It is highly recommended for stress analysis of complicated structures and/or loadings. Being non-destructive, the method allows models to be used time and again, under a variety of loadings.

Finally, one of the most important advantages of photoelasticity is the photographed contour pattern itself. A photo like Fig. 6.1 is a quite impressive experimental result. It gives an experimenter a tangible and attractive data form to supplement his report. It gives observers a better feeling as to "whats going on" than numbers by themselves.

Brittle Specimen Failure

The results of the brittle specimen failure were poor. Microscopic stress concentrations in the cast iron overrode the SCF at the V notch

root. This is enough evidence to recommend that cast iron not be used in future brittle failure tests.

References cited in Chapter 2 reflect successes with brittle specimen failure. These experimenters used graphites, PMMA, and plaster-of-paris. Plaster-of-paris or other brittle mortar seems applicable to the SCF program.

However, brittle failure is not recommended for future testing. Specimen destruction runs costs high. More importantly, only the highest SCF can ever be investigated for a given geometry.

Brittle Coating

Advocates of the brittle lacquer or brittle coating method boast of its usefulness. It is marketed as a whole-field, non-destructive, quantitative, experimental stress analysis method. It is also said to be portable and inexpensive. The results of tests contained in this volume are disappointing.

Many things were tried to improve results. These fruitless efforts were documented in Chapter 4. Even if the method had performed as hoped, there are many problems with it. Prevailing atmospheric conditions greatly affect results. Careful logging of temperatures and humidities is burdening. Best results under ideal conditions result in about ±15% error [15]. The method is not recommended for future SCF determination. The problems experienced here may be reflected in the fact that one of the two United States vendors of brittle coating has withdrawn from the market in 1988.

Brittle coating technology has been delivered a blow by the

Environmental Protection Agency. New research must be done to verify the usefulness of the presently-available lacquers. Until then, this method is perhaps reduced to a role of qualitative analysis.

Moire Interferometry

Moire interferometry shows great promise as an experimental method. The SCF found for the V groove closely matches the value found by strain gaging. The spatial resolution exceeded that of the related FEA work. The displacement pattern produced (Fig. 5.4) is as impressive and as beautiful as any photoelastic pattern. The method is non-destructive and full field. Specimens can be used time and again. Regions of greatest strain can be easily spotted.

Initial costs are comparable to photoelastic set-up costs. The major problems of Moire stem from its relative youth as an experimental method. First, there are few experts with whom to consult. Similarly, gratings of proper quality are rare or not commercially available at all. There also exists a great need for automated data digitization if Moire is to be used on a large scale.

The resolution of Moire interferometry is superb. One must remember, however, that the pattern produced is displacement, not stress or strain. The accuracy of this method is diminished by digitization and strain approximations. It is the best high-grade method for full field deflection data acquisition. It seems that such a method would be ideal to use in combination with finite element analysis. The deflection data of Moire could be used as boundary conditions for FEA. This hybrid combination shows great promise.

Other Methods

S.P.A.T.E.® is an up-and-coming tool of experimental mechanics. However, advocates must first address certain questions in the engineering community. Concerns have been raised about the great dependence on known surface emissivity. One expert recommends Krylon® ultra flat black spray paint to eliminate emissive irregularities. It is awkward to sell a $185,000 stress detection device whose results depend greatly upon a $3 can of spray paint. This author does not doubt the effectiveness of the Krylon®, but the engineering world must get used to the idea.

Acoustic emission and exo-electron emission are yet to earn their wings as experimental methods. Very little data or instructions exist to assist the practical experimenter. More work must be done if these two methods are to receive even moderate use.

Conclusions

Several improvements can be made in the field of strain gage technology. Available adhesives are expensive and difficult to use. A quicker drying cement would speed work and thus cut costs. Computer software and hardware that would allow direct strain gage/computer interface would advance the field. With such an arrangement, stress concentration factors could be known almost immediately. This could eliminate costly retests.

If an experimenter knows where the point of peak stress is and wishes to quantify it, strain gages (gage length < radius/3) are recommended. If a full-field stress pattern is desired, photoelastic methods should be used.

REFERENCES

1. Jane's Fighting Ships 1988-89, Jane's Publishing Company, LTD, London, 1988.

2. Mitchell, L. D., Personal Interview, July 1988, Blacksburg, VA.

3. Shigley, J., and L. D. Mitchell, Mechanical Engineering Design, McGraw-Hill, New York, 1983.

4. Sors, L., Fatigue Design of Machine Components, Pergamon Press, 1971.

5. Hetenyi, M., Handbook of Experimental Stress Analysis, John Wiley and Sons, Inc., New York, 1950, p. 637.

6. Bach, C., "Elastizitat und Festigkeit," Julius Springer, Fifth Edition, Berlin, 1905.

7. Frocht, M., "The Behavior of a Brittle Material at Failure," Journal of Applied Mechanics, Vol. 58, pp. A99-A103, 1936.

8. Peterson, R, "An Investigation of Stress Concentration by Means of Plaster of Paris Specimens," Mechanical Engineering, Vol. 48, pp. 1449-1452, 1926.

9. Williams, J., and P. Ewing, "Fracture Under Complex Stress - The Angled Crack Problem," Int. Journal of Fracture Mechanics, Vol. 8, pp. 441-446, 1972.

10. Wu, H., R. Yao, and M. Yip, "Experimental Investigation of the Angles Elliptic Notch Problem in Tension," Journal of Applied Mechanics, Vol. 45, No. 9, pp. 455-461, 1977.

11. Theocaris, P., "Local Yielding Around a Crack Tip in Plexiglas," Journal of Applied Mechanics, Vol. 38, No. 6, pp. 409-415, 1970.

12. Cotterell, B., "Brittle Fracture in Compression," Int. Journal of Fracture Mechanics, Vol. 8, pp. 195-208, 1972.

13. Eggeman, G., "Biaxial Failure Testing of a Transverse Isotropic Brittle Material," Proceedings of the VIII International Conference on Experimental Stress Analysis, Amsterdam, The Netherlands, May 12-16, 1986.

14. deForest, A. V., "A New Method of Measuring Strain Distribution - Brittle Coatings," Instruments, p. 113, April 1939.

15. deForest, A. V., and G. Ellis, "Brittle Lacquers as an Aid to Stress Analysis," Journal of the Aeronautical Sciences, pp. 205-208, Vol. 7, 1940.

16. deForest, A. V., G. Ellis, and F. Stern, "Brittle Coatings for Quantitative Strain Measurements," Journal of Applied Mechanics, pp. A-184 to A-188, December 1942.

17. Hetenyi, M., and W. Young, "Application of the Brittle Lacquer Method in the Stress Analysis of Machine Parts," Experimental Stress Analysis, Vol. 1, pp. 116-129, 1944.

18. Durelli, A. J., and A. S. Kobayashi, "Stress Distributions Around Hydrostatically Loaded Circular Holes in the Neighborhood of Corners," Journal of Applied Mechanics, pp. 178-183, June 1958.

19. Kikukawa, M., "Factors of Stress Concentration for Notched Bars Under Tension and Bending," Proceedings of the 10th International Congress of Applied Mechanics, Stresa, Italy, 1960, pp. 337-341, 1962.

20. Watanabe, O., and Y. Izumi, "An Experiment on a New Type of Resistance Foil Strain Gage for Analysis of Concentrated Stresses," Semiconductor and Conventional Strain Gages, M. Dean, Ed., pp. 21-44, 1962.

21. Dally, J. W., and R. J. Sanford, "Strain-Gage Methods for Measuring the Opening Mode Stress-Intensity Factor, K_I," Experimental Mechanics, pp. 381-388, December 1987.

22. Dally, J. W., and W. Riley, Experimental Stress Analysis, McGraw-Hill, 1978.

23. Neumann, F. E., "Die Gesetze der Doppelbrechung des Lichts in Comprimierten oder Ungleichfor-mig Erwarmten Unkrystallinischen Korpern," Abh. K. Acad. Wiss. Berlin, Pt. II, pp. 1-254, 1841.

24. Maxwell, J. C., "On the Equilibrium of Elastic Solids," Trans. R. Soc. Edinburgh, Vol. XX, Part 1, pp. 87-120, 1853.

25. Frocht, M. M., "Recent Advanced in Photoelasticity and an Investigation of the Distribution in Square Blocks Subjected to Diagonal Compression," Transactions ASME, Applied Mechanics Division, Vol. 53, No. 15, October 1931.

26. Coker, E. G., General Electric Review, November and December 1920; January, March, and May 1921 (Five Articles).

27. Frocht, M. M., "Photoelastic Studies in Stress Concentration," Mechanical Engineering, Vol. 58, August 1936.

28. Frocht, M. M., "The Behavior of a Brittle Material at Failure," Journal of Applied Mechanics, Vol. 3, No. 3, September 1936.

29. Frocht, M. M., and H. N. Hill, "Stress Concentration Factors Around a Central Circular Hole in a Plate Loaded Through a Pin in the Hole," Journal of Applied Mechanics, Vol. 7, No. 1, March 1940.

30. Frocht, M. M., and M. M. Leven, "Factors of Stress Concentration for Slotted Bars in Tension and Bending," Journal of Applied Mechanics, Vol. 18, No. 1, March 1951.

31. Frocht, M. M., and D. Landsberg, "Factors of Stress Concentration in Bars with Deep Shart Grooves and Fillets in Tension," Proceedings of the Society for Experimental Stress Analysis, Vol. 8, No. 2, 1951.

32. Frocht, M. M., and M. M. Leven, "Stress Concentration Factors for Single Notch in Flat Bar in Pure and Central Bending, Journal of Applied Mechanics, Vol. 19, No. 4, December 1952.

33. Durelli, A. J., and W. F. Riley, "Stress Distribution on the Boundary of a Circular Hole in a Large Plate During Passage of a Stress Pulse of Long Duration," Journal of Applied Mechanics, Vol. 28, No. 2, June 1961.

34. Theocaris, P. S., and E. E. Edoutos, "A Photoelastic Determination of K_I Stress Intensity Factors," Engineering Fracture Mechanics, Vol. 7, 1975.

35. Hanus, J. B., and C. P. Burger, "Stress Concentration Factors for Elliptical Holes Near an Edge," Experimental Mechanics, September 1981.

36. Tuzi, Z., "Photoelastic Study of Stress in a Heat Treated Column," Scient. Pap. Inst. Phys. Chem. Res., Tokyo, Vol. 7, p. 104, 1927.

37. Hetenyi, M., "The Fundamentals of Three Dimensoinal Photoelasticty," Journal of Applied Mechanics, Vol. 5, No. 4, pp. 149-154, December 1938.

38. Drucker, D., and R. D. Mindlin, "Stress Analysis by Three-Dimensional Photoelastic Methods," Journal of Applied Physics, Vol. 11, pp. 724-732, 1940.

39. Frocht, M. M., "Studies in Three-Dimensional Photoelasticity - Stress Concentrations in Shafts with Transverse Circular Holes in Tension; Relation Between Two and Three-Dimensional Factors," Journal of Applied Physics, Vol. 15, No. 1, pp. 72-88, January 1944.

40. Leven, M., "Stresses in Keyways by Photoelastic Methods and Comparison with Numerical Solution," Proceedings SESA, Vol. 7, No. 2, pp. 141-154, 1950.

41. Hartman, J., and M. Leven, "Factors of Stress Concentration for the Bending Case of Fillets in Flat Bars and Shafts with Center Enlarged Section," Proceedings SESA, Vol. 9, No. 1, p. 53, 1951.

42. Fessler, H., and E. Roberts, "Bending Stresses in a Shaft with a Transverse Hole," Selected Papers on Stress Analysis, Chapman and Hall, London, pp. 45-49, 1961.

43. Marloff, R., M. Leven, T. Ringler, and R. Johnson, "Photoelastic Determination of Stress Intensity Factors," Experimental Mechanics, December 1971.

44. Sanford, R., and L. Beaubien, "Stress Analysis of a Complex Part: Photoelasticity vs. Finite Elements," Experimental Mechanics, December 1977.

45. Smith, C. W., J. J. McGowan, and W. H. Peters, "A Study of Crack Tip Non-Linearities in Frozen Stress Fields," Experimental Mechanics, Vol. 18, No. 8, pp. 309-315, August 1978.

46. Smith, C. W., "Photoelastic Determination of Stress Intensity Factors," Mechanics of Fracture, Vol. III, Experimental Fracture Mechanics, G. C. Shih, Ed., Sisthoff & Nordhoff International, 1980.

47. Smith, C. W., W. H. Peters, and S. F. Gou, "Influence of Flaw Geometries on Hole Crack Stress Intensities," Fracture Mechanics ASTM STP 677, pp. 431-448, October 1979.

48. Smith, C. W., "Stress Intensity and Flaw Shape Variations in Surface Flaws," Experimental Mechanics, Vol. 20, No. 4, pp. 126-133, April 1980.

49. Post, Manual on Experimental Stress Analysis, Edited by W. Tuppeny and A. Kobayashi, Second Edition, Chapter 4, pp. 29-48, Westport, Conn., SESA, 1965.

50. Burger, "Photoelasticity," Handbook on Experimental Mechanics, ed. by A. Kobayashi, Prentice-Hall, Englewood Cliffs, NJ, 1987.

51. Guild, J., The Interference Systems of Crossed Diffraction Gratings, Clarendon Press, London, 1956.

52. Underwood, J., and D. Kendall, "Measurement of Microscopic Plastic-Strain Distribution in the Region of a Crack Tip," Experimental Mechanics, Vol. 9, No. 7, pp. 296-304, 1969.

53. Post, D., "Optical Interference for Deformation Measurements -- Classical, Holographic and Moire Interferometry," Mechanics of Nondestructive Testing, Ed. by W. W. Stinchcomb, Plenum Publishing, pp. 1-53, 1980.

54. Hiatt, G., "Experimental Determination of Stress Intensity Factors Using Moire Interferometry," M.S. Thesis, Virginia Polytechnic Institute and State University, Engineering Science and Mechanics, Blacksburg, VA, 1981.

55. Basehore, M., and D. Post, "Moire Method for In-Plane and Out of Plane Displacement Measurements," Experimental Mechanics, Vol. 21, No. 9, pp. 321-328, 1981.

56. Nicoletto, G., "Experimental Determination of Stress Intensity Factors by Optical Methods," M.S. Thesis, Virginia Polytechnic Institute and State University, Engineering Science and Mechanics, Blacksburg, VA, 1981.

57. Sciammarella, C., "The Moire Method - A Review," Experimental Mechanics, Vol. 22, No. 11, pp. 418-433, 1982.

58. Watson, R., and D. Post, "Precision Strain Standard by Moire Interferometry for Strain-Gage Calibration," Experimental Mechanics, Vol. 22, No. 7, pp. 256-261, 1982.

59. Smith, C. W., D. Post, G. Hiatt, and G. Nicoletto, "Displacement Measurements Around Cracks by a Hybrid Experimental Technique," Experimental Mechanics, Vol. 23, No. 1, pp. 15-20, 1983.

60. Smith, C. W., D. Post, and G. Nicoletto, "Experimental Stress-Intensity Distributions in Three-Dimensional Cracked-Body Problems," Experimental Mechanics, Vol. 23, No. 12, pp. 378-382, 1983.

61. Post, D., R. Czarnek, and C. W. Smith, "Patterns of U and V Displacements Around Cracks in Aluminum by Moire Interferometry," Application of Fracture Mechanics to Materials and Structures, ed. by G. Sih, Martinus Nijhoff Publishers, Boston, 1984.

62. Ruiz, C., D. Post, and R. Czarnek, "Moire Interferometric Study of Dovetail Joints," Journal of Applied Mechanics, Vol. 53, No. 3, pp. 109-114, 1985.

63. Post, D., "Moire Interferometry," Handbook on Experimental Mechanics, ed. by A. Kobayashi, Prentice-Hall, Englewood Cliffs, NJ, 1987.

64. Oliver, D., "Stress Pattern Analysis by Thermal Emission," Handbook on Experimental Mechanics, ed. by A. Kobayashi, Prentice-Hall, Englewood Cliffs, NJ, 1987.

65. Biot, M. A., "Plasticity and Consolidation in a Porous Anisotropic Solid," Journal of Applied Physics, Vol. 26, 1955.

66. Biot, M. A., "Thermoelasticity and Irreversible Thermodynamics," Journal of Applied Physics, Vol. 27, 1956.

67. Biot, M. A., "Irreversible Thermodynamics with Application to Viscoelasticity," Physics Review, Vol. 97, 1955.

68. Mountain, D. S., and J. M. B. Webber, "Stress Pattern Analysis by Thermal Emission (S.P.A.T.E.®)," Proceedings of 4th European Electro-Optics Conference, Utrecht, Netherlands, Vol. 164, pp. 189-196, 1978.

69. Stanley, P., and W. K. Chan, "Quantitative Stress Analysis by Means of the Thermoelastic Effect," Proceedings of the 5th International Congress on Experimental Mechanics, Montreal, pp. 547-554, 1984.

70. Dandliker, R., and B. Ineichen, "Quantitative Strain Measurement Through Holographic Interferometry," Proceedings of the Third European Electro-Optics Conference and Exhibition, Geneva, SPIE, Vol. 99, 1976.

71. Dudderar, T., and R. O'Regan, "Measurement of the Strain Field Near a Crack Tip in Polymethylmethacrylate by Holographic Interferometry," Experimental Mechanics, Vol. 11, pp. 49-56, 1971.

72. Dudderar, T., and H. Gorman, "The Determination of Mode I Stress-Intensity Factors by Holographic Interferometry," Experimental Mechanics, Vol. 19, pp. 145-149, 1979.

73. French, D., and B. MacDonald, "Experimental Methods of X-Ray Stress Analysis," Experimental Mechanics, Vol. 9, pp. 456-462, October 1969.

74. Rowlands, R., "Residual Stresses," Handbook of Experimental Mechanics, ed. by A. Kobayashi, Prentice-Hall, Englewood Cliffs, NJ, pp. 768-813, 1987.

75. Nolan, I., and J. Cohen, Residual Stress, Springer-Verlag, 1987.

76. Kosmatka, J., S. Ligore, and P. Stiles, Unpublished Finite Element Work, Virginia Polytechnic Institute and State University, Mechanical Engineering Department, 1988.

77. Fries, R. H., Unpublished Work, Virginia Polytechnic Institute and State University, Mechanical Engineering Department, 1988.

78. Fries, R. H., and M. Biegler, Unpublished Work, Virginia Polytechnic Institute and State University, Mechanical Engineering Department, 1988.

APPENDIX A

Table A.1 Results of Strain Gage SCF Work with Comparison to Finite Element Results

Notes: 1. For all specimens $r_u/t = 0.1$ and $r_v/t = 0.0308$.
2. Drawings are not to scale.

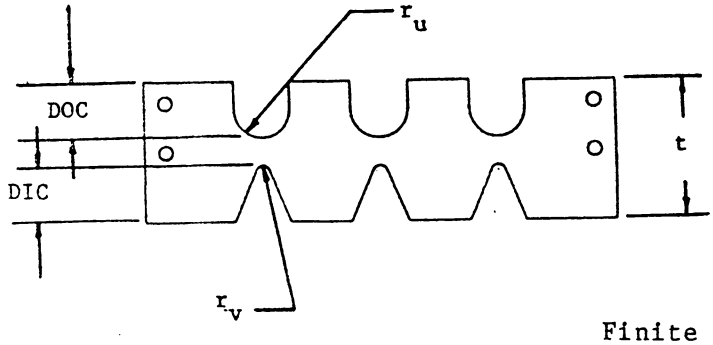

		Strain Gage	Finite Element Analysis
A1 Double U DOC/t = .4	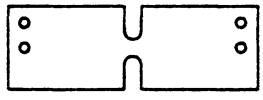	K_T = 1.68 K_B = 1.26	K_T = not avail.
A2 Double U DOC/t = .2	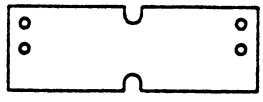	K_t = 2.37 K_B = 1.88	K_t = 2.45
A3 Double V DIC/t = .3	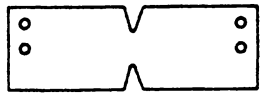	K_t = 3.50 K_B = 2.40	K_t = not avail.
A4 Double V DIC/t = .2	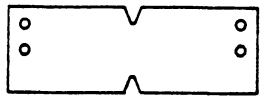	K_T = 3.97 K_B = 2.91	K_T = not avail.

Table A.1 (continued)

A5 UV DIC/t = .1 DOC/t = .6	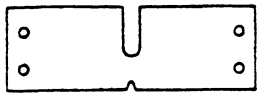	$K_t(U) = 1.92$ $K_t(V) = 2.98$ $K_B(U) = 1.40$ $K_B(V) = 2.29$	$K_t(U) = 1.93$ $K_t(V) = 2.52$
A6 UV DIC/t = .1 DOC/t = .2	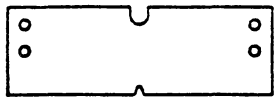	$K_t(U) = 2.54$ $K_t(V) = 2.94$ $K_B(U) = 2.06$ $K_B(V) = 2.98$	$K_t(U) = 2.48$ $K_t(V) = 3.4$
A7 UV DIC/t = .3 DOC/t = .6	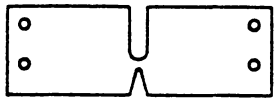	$K_t(U) = 1.32$ $K_t(V) = 1.68$ $K_b(U) = 1.08$ $K_b(V) = 1.50$	$K_t(U) = 1.35$ $K_t(V) = 1.60$
A8 UV DIC/t = .3 DOC/t = .2	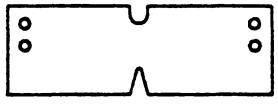	$K_t(U) = 2.32$ $K_t(V) = 3.84$ $K_B(U) = 1.76$ $K_B(V) = 3.12$	$K_t(U) = 2.35$ $K_t(V) = 3.30$

APPENDIX B

```
10 REM  PROGRAM 1.  EVALUATES DATA TO FIND AXIAL STRESS CONCENTRATION FACTORS
20 REM
30 REM
40 REM
50 CLS
60 TOTL=0
70 TOTR=0
80 REM    THIS PROGRAM MODIFIED AS OF 27 APRIL 1988
90 PRINT "THIS PROGRAM DEVELOPED TO REDUCE DATA TAKEN FROM STRAIN"
100 PRINT "GAUGE SPECIMENS FOR THE NSWC/DL PROJECT"
110 PRINT : PRINT
120 PRINT "PLEASE ENTER DATE OF TEST:"
130 INPUT A$
140 PRINT "PLEASE ENTER EXPERIMENTER(S)"
150 INPUT B$
160 PRINT "SPECIMEN:"
170 INPUT SPEC$
180 CLS
190 PRINT "****************** SIMPLE TENSION CASE **********************"
200 PRINT
210 PRINT "PLEASE ENTER THE NUMBER OF LOADS USED IN THIS CASE:"
220 INPUT N
230 PRINT "ENTER LOADS, LEFT GAUGE READING, & RIGHT GAUGE READING AS REQUESTED"
240 FOR X = 1 TO 4000
250 NEXT X
260 CLS
270 FOR L = 1 TO N
280 PRINT "LOAD ";L;" (POUNDS):"
290 INPUT P(L)
300 PRINT
310 PRINT "LEFT GAUGE READING AT THIS LOAD (MICROSTRAIN):"
320 INPUT LGR(L)
330 PRINT
340 PRINT "RIGHT GAUGE READING AT THIS LOAD (MICROSTRAIN):"
350 INPUT RGR(L)
360 FOR X = 1 TO 1200
370 NEXT X
380 CLS
390 NEXT L
400 CLS
410 PRINT "SPECIMEN GEOMETRY"
420 PRINT "ENTER SPECIMEN THICKNESS:"
430 INPUT T
440 PRINT "ENTER THROAT WIDTH:"
450 INPUT TW
460 A = T * TW
470 FOR L = 1 TO N
480 SFL(L)=(10.35*LGR(L))/(P(L)/A)
490 SFR (L)=(10.35*RGR(L))/(P(L)/A)
500 TOTL=TOTL+SFL(L)
510 TOTR=TOTR+SFR(L)
520 NEXT L
530 AVR=TOTR/N
540 AVL=TOTL/N
550 CLS
560 PRINT "$$$$$$$$$     STRESS CONCENTRATION FACTORS       $$$$$$$"
570 PRINT:PRINT
580 PRINT "P#   SCF (LEFT GAUGE)          SCF(RIGHT GAUGE)             SCF(AVG)
590 FOR L = 1 TO N
600 PRINT L;"    "SFL(L);"                  ";SFR(L);"                   ";AVG(L)
```

```
610 NEXT L
620 PRINT "PRESS ENTER WHEN PRINTER IS READY"
630 INPUT NOTIN
640 LPRINT "                              NSWC/DL"
650 LPRINT "                STRESS CONCENTRATION FACTORS"
660 LPRINT:LPRINT:LPRINT
670 LPRINT "TEST DATE:  ";A$
680 LPRINT "EXPERIMENTER(S)  :";B$
690 LPRINT "SPECIMEN:";SPEC$
700 LPRINT:LPRINT:LPRINT
710 LPRINT"LOAD        SCF(LEFT)            SCF(RIGHT)                "
720 FOR L = 1 TO N
730 LPRINT P(L);"      ";SFL(L);"            ";SFR(L)
740 NEXT L
750 LPRINT
760 LPRINT "average:     ";AVL;"            ";AVR
770 PRINT "enter 1 to print again"
780 INPUT CHECK
790 IF CHECK=1 THEN 620
```

```
10 REM  PROGRAM 2.     EVALUATES BENDING STRESS CONCENTRATION FACTORS
20 REM
30 REM
40 REM
50 DIM H(9), B(9)
60 SUM=0
70 SUM2=0
80 REM this PROGRAM CREATED IN MARCH 88 BY MARK BIEGLER
90 REM TO FIND BENDING STRESS CONCENTRATION FACTORS FOR NSWC/DL
100 CLS
110 PRINT "   BENDING STRESS CONCENTRATION FACTORS   "
120 PRINT: PRINT
130 PRINT "ENTER DATE OF TEST:"
140 INPUT D$
150 PRINT
160 PRINT "ENTER NAMES OF EXPERIMENTERS:"
170 INPUT N$
180 PRINT
190 PRINT "ENTER SPECIMEN DESCRIPTION"
200 INPUT Z$
210 PRINT "IF SPECIMEN IS SYMMETRIC, ENTER 1"
220 PRINT "IF SPECIMEN IS NOT SYMMETRIC, ENTER 2"
230 INPUT CHECK
240 FOR R= 1 TO 200
250 NEXT R
260 CLS
270 PRINT "ENTER LOAD"
280 INPUT P
290 PRINT "ENTER THROAT WIDTH"
300 INPUT TW
310 PRINT "ENTER ECCENTRICITY"
320 INPUT EX
330 PRINT:PRINT
340 PRINT "HOW MANY PULLS?"
350 INPUT PULLS
360 PRINT "ENTER STRAINS ON FIRST NOTCH"
370 FOR I = 1 TO PULLS
380 INPUT H(I)
390 SUM = H(I)+SUM
400 NEXT I
410 E=SUM/PULLS
420 PRINT "ENTER AXIAL STRESS CONCENTRATION FACTOR AT CONCERNED NOTCH"
430 INPUT KT
440 NUM=10.35*E-KT*4*P/TW
450 DEN=24*P*EX/(TW*TW)
460 KB=NUM/DEN
470 KB=ABS (KB)
480 PRINT "KB= ";KB
490 REM OTHER SIDE
500 CLS
510 PRINT "OTHER SIDE"
520 PRINT "ENTER STRAINS"
530 FOR I = 1 TO PULLS
540 INPUT B(I)
550 SUM2=B(I)+SUM2
560 NEXT I
570 E2 =SUM2/PULLS
580 PRINT "ENTER AXIAL STRESS CONCENTRATION FACTOR AT THIS NOTCH"
590 INPUT KT2
600 NUM2=10.35*E2-KT2*4*P/TW
```

```
610 KB2=NUM2/DEN
620 KB2= ABS(KB2)
630 PRINT "KB2=";KB2
640 IF CHECK = 2 GOTO 860
650 CLS
660 AVG=(KB+KB2)/2
670 PRINT "SYMMETRIC SPECIMEN"
680 PRINT :PRINT
690 PRINT "HIT ENTER WHEN PRINTER IS READY"
700 INPUT NUTHIN
710 LPRINT:LPRINT
720 LPRINT "###################    BENDING STRESS CONCENTRATION FACTORS    #####
#######"
730 LPRINT "                                    NSWC/DL PROJECT"
740 LPRINT:LPRINT
750 LPRINT Z$
760 LPRINT D$
770 LPRINT N$
780 LPRINT : LPRINT
790 LPRINT "KB="
800 LPRINT AVG
810 PRINT "ENTER 1 FOR ANOTHER PRINT:"
820 INPUT FRI
830 IF FRI=1 GOTO 710
840 PRINT KB;"               ";KB2
850 END
860 PRINT "NON - SYMMETRIC SPECIMEN"
870 INPUT UIO
880 PRINT:PRINT
890 LPRINT "********************BENDING STRESS CONCENTRATION FACTORS************
******"
900 LPRINT:LPRINT
910 LPRINT "                                NSWC/DL PROJECT"
920 LPRINT:LPRINT
930 LPRINT D$
940 LPRINT N$
950 LPRINT Z$
960 LPRINT:LPRINT
970 PRINT KB;"                    ";KB2
980 LPRINT "   KB LEFT                      KB RIGHT"
990 LPRINT "    ";KB;"                       ";KB2
1000 PRINT "ENTER 1 FOR ANOTHER PRINT"
1010 INPUT PRI
1020 IF PRI= 1 GOTO 880
1030 END
```

The vita has been removed from the scanned document